Research Square

Preprints are preliminary reports that have not undergone peer review.
They should not be considered conclusive, used to inform clinical practice,
or referenced by the media as validated information.

Programmable and reversible protein degradation via G-quadruplex assembled PROTACs for cancer therapy

Yan Xu

xuyan@med.miyazaki-u.ac.jp

University of Miyazaki https://orcid.org/0000-0003-0379-8866

Shiyu Wang

University of Miyazaki

Hisao Saneyoshi

University of Miyazaki

Haruki Fujita

Tokyo University of Agriculture and Technology

Kazuo Nagasawa

Article

Keywords:

Posted Date: April 2nd, 2026

DOI: https://doi.org/10.21203/rs.3.rs-9143133/v1

License: This work is licensed under a Creative Commons Attribution 4.0 International License.
Read Full License

Additional Declarations: There is **NO** Competing Interest.

Programmable and reversible protein degradation via G-quadruplex assembled PROTACs for cancer therapy

Shiyu Wang[1], Hisao Saneyoshi[1], Haruki Fujita[2], Kazuo Nagasawa[2] and Yan Xu[1,*]

[1]Division of Chemistry, Department of Medical Sciences, Faculty of Medicine, University of Miyazaki, 5200 Kihara, Kiyotake, Miyazaki 889-1692, Japan

[2]Tokyo University of Agriculture and Technology,
Department of Technology
2-24-16 Naka-cho, Koganei, Tokyo 184-8588, Japan

*To whom correspondence should be addressed. Tel: +81-985-85-0993;
Email: xuyan@med.miyazaki-u.ac.jp

Abstract

Developing proteolysis-targeting chimeras (PROTACs) as universal platforms for efficient and controllable protein degradation remains a major challenge. Here we report a non-covalent G-quadruplex framework–based PROTAC strategy, termed G4TACs. Inspired by the structural stability, programmability, and editability of G-quadruplexes, this platform integrates conventionally synthesized oligonucleotides with G4–ligand interactions to assemble modular degradation complexes that recruit both a BRD4-binding ligand (JQ1) and the E3 ligase recruiter pomalidomide. G4TACs enable multivalent assembly of degradation complexes directly inside cells and induce potent BRD4 degradation. Importantly, antisense oligonucleotides allow reversible regulation of G4 folding and unfolding, enabling switchable on–off assembly of the BRD4–G4–cereblon complex and dynamic control of protein degradation. Functionally, G4TAC-induced BRD4 degradation triggers apoptosis and robust inhibition of cancer cell proliferation, and exhibits strong antitumor activity in an adrenocortical carcinoma xenograft model. Furthermore, repurposing the FDA-approved kinase inhibitor ceritinib enables efficient ALK degradation, demonstrating the versatility of this strategy. Together, these findings establish G4TACs as a programmable and reversible platform for targeted protein degradation with broad therapeutic potential.

Introduction

Targeted protein degradation has emerged as a promising therapeutic strategy, with proteolysis targeting chimeras (PROTACs) representing one of the most powerful modalities[1-4]. PROTACs are heterobifunctional molecules composed of a ligand for the protein of interest (POI), an E3 ligase–recruiting moiety (E3LRM), and a linker that connects these two components. Recent studies have revealed that the linker is not a passive connector but a critical determinant of PROTAC activity, as it governs the spatial arrangement, dynamics, and stability of the ternary complex formed between the POI and the E3LRM[5-7].

To date, a wide range of conventional linkers, including polyethylene glycol (PEG)[8], linear aliphatic chains[9], and more rigid piperazine-type motifs[5], have been extensively explored. However, intrinsic limitations of these linkers severely constrain PROTAC performance. Rigid linkers can lead to unstable POI engagement, whereas highly flexible linkers may introduce excessive conformational freedom, resulting in reduced degradation efficiency or drug resistance[10]. Moreover, structure–activity relationship (SAR) optimization of linker length and composition remains largely empirical, requiring extensive synthetic and biological screening[8]. In some cases, arbitrarily selected linker lengths are inevitably adopted, which compromises therapeutic efficacy[11]. Therefore, developing intelligent linker architectures with precise control over length, orientation, and connectivity remains a central challenge for next-generation PROTAC design[6].

Considerable efforts have been devoted to overcoming linker-related limitations. Multivalent PROTACs, such as trivalent architectures, have been reported to enhance degradation potency; however, their fully covalent assembly imposes substantial synthetic burdens[12-14]. Alternatively, DNA tetrahedra have been explored as scaffolds for loading multiple ligands, including small molecules, aptamers, and antibodies. Nevertheless, their large size and redundant DNA sequences often induce immunogenicity and rapid clearance *in vivo*, limiting translational applications[15]. Bioorthogonal click chemistry–based self-assembly strategies have also been developed, yet their low aqueous solubility and slow reaction kinetics impede broader utility[16]. Consequently, an efficient, biocompatible, and modular platform capable of organizing multiple warheads with high spatial precision is still urgently needed.

Over the past decades, G-quadruplex (G4) structures have emerged as robust bioengineering materials in biophysics and medicinal chemistry, enabling applications such as allosteric regulation of DNA nanostructures and cancer-selective drug delivery[17-19]. These functions arise from several intrinsic advantages of G4s, including high stability under physiological conditions, tunable spatial configurations, and versatile interactions with small-molecule ligands. Importantly, numerous G4 ligands have been reported to bind G4s with high affinity through diverse interaction modes, including π–π stacking on G-tetrad planes, groove or loop binding, and electrostatic or hydrogen-bonding interactions, with defined orientation and binding topology[20-22]. Collectively, these properties endow G4s with platform-like potential for organizing functional molecules in a programmable manner.

Here, we exploit these features to establish a non-covalent G-quadruplex framework–based PROTAC platform (G4TACs) (Fig. 1). As a proof of concept, we design *de novo* G4TAC assemblies using bimolecular G4 scaffolds and G4–ligand conjugates that enable precisely programmable multivalent architectures, allowing POI to E3LRM stoichiometries of 1:1, 2:1 and 4:1 through rational variation of G4 scaffolds and G4–ligand conjugates, thereby achieving enhanced protein degradation efficacy (Fig. 1). Using the bromodomain and extraterminal (BET) family protein BRD4 as a model, we demonstrate that G4TACs induce robust and efficient protein degradation.

A distinctive advantage of the G4TAC strategy is its reversible and spatiotemporally controllable regulation of protein degradation. By employing antisense oligonucleotides to regulate G4 folding and unfolding, we achieve switchable “on” and “off” assembly of active G4TAC complexes, enabling controlled degradation and recovery of target proteins (Fig. 1).

This reversibility provides a new approach to precisely and periodically modulate anticancer activity while mitigating the on-target toxicity associated with conventional irreversible PROTACs.

Functionally, G4TAC-mediated BRD4 degradation triggers pronounced apoptotic responses, resulting in strong inhibition of cancer cell proliferation and induction of cell death. We further validate the therapeutic potential of G4TACs in an adrenocortical carcinoma xenograft mouse model, where efficient BRD4 degradation and significant tumor growth suppression are observed *in vivo* (Fig. 1). To demonstrate the generality of this platform, we repurpose the FDA-approved ALK inhibitor ceritinib to construct G4TACs targeting ALK, achieving more potent protein degradation than previously reported approaches[23].

Together, these results establish G4TACs as a programmable, modular, and reversible PROTAC platform, in which "LEGO-like" G4-based assemblies enable superior and controllable protein degradation, offering a new paradigm for targeted protein degradation and diverse therapeutic applications.

Results

Design and synthesis of Bi-G4

To construct the G4-based platform, we employed a well-established bimolecular G-quadruplex (Bi-G4) architecture formed through G-tetrad–mediated intermolecular interactions between two G-rich DNA strands[24,25]. Specifically, a short 6-mer strand and a longer 16-mer strand were designed to assemble into a bimolecular G-quadruplex structure (Fig. 2a and Supplementary Table 1), based on our previous studies demonstrating stable G4 formation from paired G-rich sequences[26,27]. To further enhance the stability of the Bi-G4 scaffold, 8-trifluoromethyl-2′-deoxyguanosine (^{F}G) was incorporated into the G-rich sequences (Fig. 2a). This modification is known to preferentially adopt a *syn* glycosidic conformation, thereby promoting and stabilizing G-quadruplex formation and improving the thermodynamic stability of the assembled structure[28].

For construction of the PROTAC-like system, the BRD4 inhibitor JQ1 and the E3 ligase ligand pomalidomide (Pm), both widely used components in PROTAC design[29,30], were conjugated to the DNA oligonucleotides to generate the G4-based PROTAC constructs (G4TACs) (Fig. 2b). To achieve optimal degradation efficiency, linkers of varying lengths connecting JQ1 and pomalidomide (Pm) to the DNA scaffold were designed and evaluated, as the linker length determines the spatial distance between JQ1 and Pm and thus strongly influences their interactions with the target protein and E3 ligase (Fig. 2c).

Computation-assisted molecular dynamics (MD) simulations revealed that the Bi-G4 structure with linker lengths of m,n = 3 exhibited the lowest energy (−4044.10 kcal/mol). In this configuration, the distance between Pm and JQ1 was 16.8 Å, which falls within the optimal range of 3.0–19.9 Å reported for efficient PROTAC-mediated ternary complex formation (Fig. 2d and Supplementary Table 2)[16]. Molecular docking analysis further showed the highest docking score (−78.58) for the m,n = 3 linker configuration (Fig. 2e and Supplementary Table 3), likely due to the stable G4 scaffold and favorable spatial orientation of JQ1 and Pm (Fig. 2d and 2e). Collectively, these results indicate that Bi-G4 (m,n = 3) represents the optimal configuration for subsequent studies. Based on this design,

oligonucleotides Pm-6 mer and JQ1-16 mer containing linkers with m,n = 3 were synthesized and assembled to form the Bi-G4 structure. Native PAGE analysis showed the appearance of a new band with lower electrophoretic mobility, accompanied by the disappearance of the individual Pm-6mer and JQ1-16mer bands when mixed at a 1:1 ratio, indicating the formation of a higher-order structure (Supplementary Fig. 1a). The formation of the G-quadruplex structure was further confirmed by imino proton ^{1}H NMR spectroscopy, which revealed characteristic signals in the Hoogsteen hydrogen-bonding region (10–12 ppm), consistent with G-quadruplex formation. Importantly, these signals closely resembled those observed for the native G4 structure (Fig. 2f). Circular dichroism (CD) spectroscopy further supported this conclusion, showing two positive bands at 255 nm and 290 nm**,** which are characteristic of G-quadruplex conformations (Fig. 2g). Thermal melting analysis revealed that Bi-G4 exhibits higher thermal stability than the native G4 structure, with melting temperatures (T_m) of 61.5 °C and 57.2 °C, respectively (Fig. 2h). Together, these results demonstrate that the engineered Bi-G4 scaffold forms a G-quadruplex structure similar to the native G4 but with enhanced stability.

To verify that Bi-G4 maintains its G-quadruplex structure in cells, an immunofluorescence assay was performed using the G-quadruplex-specific antibody BG4. Bi-G4 was labeled with Cy3 to enable fluorescence colocalization analysis. Compared with PBS-treated cells, which showed baseline fluorescence derived from endogenous G4 structures, cells treated with Cy3-labeled Bi-G4 exhibited significantly stronger signals that were highly colocalized with BG4 staining, confirming the presence of stable G-quadruplex structures in cells (Fig. 2i). Consistently, ^{1}H NMR analysis demonstrated that Cy3-labeled Bi-G4 retained the characteristic G-quadruplex proton signals (Supplementary Fig. 1b), indicating that the labeling did not disrupt G4 folding. Furthermore, the physiological stability of Bi-G4 was evaluated in cell lysates, where more than 40% of the structure remained intact after 72 h (Supplementary Fig. 2a). This stability is likely attributable to the enhanced resistance of the modified G4 scaffold to nuclease degradation, as reported previously[31,32].

Prior to evaluating protein degradation, we investigated whether Bi-G4 could form a ternary complex with BRD4 and the E3 ligase cereblon (CRBN). Native PAGE analysis showed a slower-migrating band when CRBN was added to Bi-G4 at a 1:1 ratio, compared with Bi-G4 alone. Upon subsequent addition of one equivalent of BRD4, an additional band shift was observed, indicating formation of a higher-order complex. No further shift occurred when two equivalents of BRD4 were added (Fig. 2j), suggesting that the complex forms with a 1:1:1 stoichiometry. The binding affinities between Bi-G4 and the proteins were further quantified using fluorescence titration assays. Dissociation constants (K_d) of 108.9 nM and 471.6 nM were obtained for BRD4 and CRBN, respectively, which are comparable to those reported for the free ligand–protein interactions (BRD4–JQ1 ≈ 90 nM and CRBN–Pm ≈ 400 nM) (Supplementary Fig. 3)[33,34]. Competitive titration experiments further showed that the presence of free ligands JQ1 or Pm significantly weakened the interactions, increasing the K_d values to 281.5 nM and 824.1 nM, respectively (Supplementary Fig. 4). Together, these results demonstrate that the G4-assembled warheads retain strong binding affinity toward their respective proteins and readily form a stable BRD4–Bi-G4–CRBN ternary complex, thereby enabling efficient initiation of PROTAC-mediated protein degradation (Fig. 3a).

Bi-G4 induces CRBN-dependent proteasomal degradation of BRD4

To determine whether Bi-G4 could induce BRD4 degradation, western blot (WB) analysis was performed to quantify BRD4 protein levels in cells treated with G4TACs. A time-course experiment showed that BRD4 levels were markedly reduced after 16 h of treatment (Supplementary Fig. 5a). We next evaluated the degradation activity of Bi-G4 using a dose-dependent assay, which revealed a DC_{50} of 7.39 nM, comparable to that of dBET1, a widely used benchmark degrader of BRD4 (Fig. 3b and Supplementary Fig. 6a)[30]. To confirm the degradation mechanism, cells were co-treated with the proteasome inhibitor MG132, which abolished the reduction of BRD4 levels (Supplementary Fig. 5b). Furthermore, excess free ligands JQ1 or pomalidomide (Pm) similarly blocked the degradation activity of Bi-G4, indicating that BRD4 degradation proceeds through a CRBN-dependent proteasomal pathway (Supplementary Fig. 5c and 5d). To verify the importance of the G-quadruplex scaffold, a control oligonucleotide (JQ1-16 mer-T) in which guanine residues were replaced by thymine was synthesized. In contrast to Bi-G4, BRD4 protein levels remained unchanged even at concentrations up to 1000 nM, demonstrating that formation of the G4 structure is essential for constructing active G4TACs capable of inducing protein degradation (Supplementary Fig. 5e).

Because G4 structures can spontaneously assemble under physiological conditions, we next investigated whether Bi-G4 could assemble in cells. BG4 immunofluorescence staining revealed weak signals corresponding to endogenous G4 structures when Pm-6mer or JQ1-16mer were introduced individually. In contrast, when cells were sequentially treated with both oligonucleotides, a strong fluorescence signal was observed, indicating in-cell assembly of the Bi-G4 structure (Fig. 3c). Consistent with this observation, BRD4 degradation was detected only when both oligonucleotides were present, whereas BRD4 levels remained largely unchanged in cells treated with either Pm-6mer or JQ1-16mer alone (Fig. 3d). These results indicate that G4TAC activity is triggered by in-cell G4 assembly, where formation of the active complex within cells enables efficient BRD4 degradation.

Reversible regulation of Bi-G4 assembly for controllable protein degradation

PROTACs promote degradation of target proteins and therefore often exhibit stronger therapeutic efficacy than traditional inhibitors. Despite these advantages, the potential for on-target, off-tumor toxicity in healthy tissues remains a major challenge for clinical application[35]. To address this issue, a variety of stimuli-responsive strategies have been developed to regulate PROTAC activity, including activation by UV light[36], X-ray irradiation[36], peroxides[36,37], enzymes[38], and bioorthogonal reactions[39,40]. However, these approaches require external or chemical stimuli that may introduce phototoxicity or chemical toxicity in physiological environments. Moreover, most existing systems provide only unidirectional regulation, typically switching protein degradation from an inactive to an active state, which limits their flexibility for therapeutic applications.

Here, we designed a reversible regulatory system based on antisense oligonucleotides (ASOs) to control Bi-G4 assembly. Specifically, an antisense strand (ASO-1) was designed to hybridize with JQ1-16mer, disrupting the G-quadruplex structure and thereby inactivating the Bi-G4 assembly. Subsequently, a second strand (ASO-2) was introduced to hybridize with ASO-1 through formation of a fully complementary duplex, which releases the JQ1-16mer

strand and restores the G4 structure, thereby reactivating Bi-G4. By alternately introducing ASO-1 and ASO-2, this modular system enables reversible switching of Bi-G4 assembly, allowing controllable activation and deactivation of G4TAC-mediated protein degradation (Fig. 4a)[41].

CD spectroscopy was first employed to monitor structural changes in Bi-G4. Upon addition of ASO-1, the characteristic positive peak at 290 nm disappeared, accompanied by the emergence of a new band at 260 nm, indicating disruption of the G-quadruplex structure and formation of an ASO-1/JQ1-16 mer duplex (Supplementary Fig. 7a). Subsequently, introduction of ASO-2 restored the G4 structure through formation of a longer ASO-1/ASO-2 duplex, as evidenced by the reappearance of the characteristic G4 signals at 260 and 290 nm. Consistently, CD melting experiments revealed an increased thermodynamic stability (T_m = 72.3 °C) upon addition of ASO-1 compared with Bi-G4 alone (T_m = 61.5 °C), confirming formation of the ASO-1/JQ1-16 mer duplex. Upon subsequent addition of ASO-2, the melting temperature decreased to 59.7 °C, indicating reassembly of the G-quadruplex structure (Supplementary Fig. 7b).

To directly visualize reversible assembly and disassembly of Bi-G4, Förster resonance energy transfer (FRET) experiments were performed. The 6-mer and 16-mer oligonucleotides were labeled with Cy3 and Cy5 dyes, respectively (Pm-6 mer-Cy3 and JQ1-16 mer-Cy5), allowing detection of FRET when the two strands are brought into proximity within the G4 structure (Fig. 4b). When Bi-G4 was formed, fluorescence spectra displayed a strong FRET emission peak at 670 nm upon excitation at 550 nm. Addition of ASO-1 resulted in a marked decrease of the 670 nm emission accompanied by a significant increase at 570 nm, indicating disruption of the G4 structure (Fig. 4b). Notably, alternating addition of ASO-1 and ASO-2 enabled reversible switching of the FRET signal between “off” and “on” states over multiple cycles. Consistent results were obtained in *in vitro* fluorescence imaging, where alternating ASO-1/ASO-2 treatments produced reversible red (“on”) and green (“off”) fluorescence transitions (Fig. 4c). Furthermore, in-cell immunofluorescence analysis revealed decreased G4 signals when Bi-G4-treated cells were exposed to ASO-1, whereas fluorescence was restored upon addition of ASO-2 (Supplementary Fig. 7c). These alternating changes mirrored the *in vitro* results, confirming that the ASO strategy enables reversible regulation of Bi-G4 assembly within cells.

Next, reversible regulation of the BRD4–Bi-G4–CRBN ternary complex was examined by PAGE analysis. Addition of ASO-1 caused disappearance of the ternary complex band and appearance of three faster-migrating bands, likely corresponding to protein–DNA complexes or unfolded oligonucleotides (Supplementary Fig. 7d). Subsequent addition of ASO-2 restored the ternary complex band with mobility identical to that observed for G4TACs, demonstrating reversible formation of the ternary complex.

Finally, BRD4 protein levels were monitored following sequential addition of ASO-1 and ASO-2 in Bi-G4-treated cells. Western blot analysis showed that ASO-1 restored BRD4 protein levels to values comparable to PBS-treated control cells after Bi-G4-induced degradation. Subsequent addition of ASO-2 again triggered BRD4 degradation (Fig. 4d). This reversible regulation could be repeated for three cycles without significant loss of activity. Collectively, these results demonstrate that the ASO–G4TAC system enables spatiotemporal control of target protein degradation through reversible regulation of G-quadruplex assembly.

Such controllable degradation may substantially reduce on-target toxicity associated with excessive protein depletion in normal cells, thereby enhancing the therapeutic potential of PROTAC-based strategies.

Trivalent Bi-G4L degrades protein with improved activity

It is well established that increasing the binding valency of PROTACs can enhance protein degradation efficiency[13,42]. To achieve this, we employed a G-quadruplex binder, the heptaoxazole derivative 7OTD, previously reported in our previous studies[43-45]. 7OTD binds to Bi-G4 and assembles into a Bi-G4–ligand conjugate (Bi-G4L), enabling the loading of two JQ1 molecules on the G4 scaffold while linking the Pm warhead through 7OTD, thereby generating a trivalent G4TAC assembly (Fig. 5a). To optimize the spatial arrangement of the ligands, the linker length between 7OTD and Pm was systematically varied to identify Bi-G4L conformations with optimal degradation activity (Supplementary Table 4). Molecular dynamics simulations revealed nearly identical distances between Pm and the two JQ1 molecules (26.70 and 26.81 Å) when a linker containing three ethyl units **(**n = 3**)** was used. Under this condition, the lowest calculated energy (–9876.06 kcal mol^{-1}) was obtained, suggesting a favorable conformation capable of simultaneously engaging two BRD4 proteins while maintaining a stable G4 structure. Subsequent molecular docking analysis further supported this design, yielding the highest docking score (–75.23) for the n = 3 linker (Supplementary Table 5 and Fig. 5c). Collectively, these results indicate that Bi-G4L with n = 3 provides the optimal configuration for further investigation.

To experimentally construct the Bi-G4L system, Pm-7OTD and Bi-G4 (JQ1) were synthesized. ^{1}H NMR titration experiments revealed gradual attenuation of imino proton signals from G1, G3, G9, and G13 residues as the ligand-to-G4 ratio increased from 1:0 to 1:1, indicating that ligand binding occurs at the terminal G-tetrad near the 5′ end, consistent with previous reports (Fig. 5b) [46]. PAGE analysis confirmed the formation of Bi-G4 (JQ1) from JQ1-6mer and JQ1-16mer strands, as evidenced by a slower migrating band (Fig. 5d). Addition of Pm-7OTD further increased the band intensity, suggesting enhanced structural stability of the resulting Bi-G4L complex (Fig. 5d). CD analysis showed a pronounced enhancement of the characteristic G4 positive band at 290 nm upon ligand binding (Fig. 5e). Consistently, CD melting experiments revealed an increased melting temperature for Bi-G4L (T_m = 66 °C) compared with Bi-G4 alone (T_m = 58 °C) (Fig. 5f), confirming that Pm-7OTD binding stabilizes the G-quadruplex structure. To examine intracellular assembly, the G4 structure was labeled with Cy3 (JQ1-6mer-Cy3). Strong G4 fluorescence signals were observed in cells treated with Bi-G4L, whereas only weak signals were detected in PBS-treated cells (Supplementary Fig. 8). Moreover, the G4 signal strongly co-localized with Cy3 fluorescence, indicating successful intracellular assembly of Bi-G4L. Next, the stoichiometry of protein binding was investigated by PAGE. Addition of CRBN resulted in a slower-migrating band corresponding to the Bi-G4L–CRBN complex. Subsequent addition of one equivalent of BRD4 produced an even slower band, consistent with formation of the BRD4–Bi-G4L–CRBN ternary complex. Notably, addition of two equivalents of BRD4 further reduced the mobility, whereas no additional shift was observed upon addition of three equivalents, indicating formation of a trivalent 2BRD4–Bi-G4L–CRBN complex (Fig. 5g).

To evaluate degradation activity, concentration-dependent immunoblotting was performed following 24 h treatment (Fig. 5h, 5i and 5j). Bi-G4L exhibited a markedly lower DC_{50} of 0.93 nM, compared with Bi-G4, reflecting the enhanced degradation potency arising from increased G4 stability and higher ligand valency (Fig. 5i, Supplementary Fig. 2b and Supplementary Fig. 6b). Time-course analysis showed substantial BRD4 degradation after 16 h, with nearly complete degradation observed after 24 h (Fig. 5j). Intracellular Bi-G4L assembly was further examined using Bi-G4 (JQ1) and Pm-7OTD. Treatment with 7OTD alone produced moderate G4 fluorescence signals, likely due to binding to endogenous G4 structures as reported previously (Supplementary Fig. 9a). As expected, introduction of Bi-G4 (JQ1) generated strong G4 fluorescence, which became significantly stronger following sequential addition of Bi-G4 (JQ1) and Pm-7OTD, confirming in-cell Bi-G4L assembly (Supplementary Fig. 9a). Consistent with this observation, western blot analysis revealed pronounced BRD4 degradation only when cells were sequentially treated with Bi-G4 (JQ1) and Pm-7OTD, whereas little degradation occurred when either component was applied individually (Supplementary Fig. 9b).

Finally, we investigated whether ASO-controlled reversible regulation could also be achieved with the trivalent Bi-G4L system, which possesses stronger degradation capacity (Supplementary Fig. 10a). CD spectroscopy showed that addition of ASO-1 abolished the G4 peak at 290 nm and produced a new band at 260 nm, indicating G4 unfolding and formation of the ASO-1/JQ1-16mer duplex (Supplementary Fig. 10b). Subsequent addition of ASO-2 restored the G4 signal at 290 nm while strengthening the 260 nm band, consistent with formation of a longer ASO-1/ASO-2 duplex and re-folding of the G4 structure. CD melting experiments further supported this mechanism. Addition of ASO-1 increased the melting temperature to 72.5 °C, compared with 66.0 °C for Bi-G4L, confirming duplex formation. Subsequent addition of ASO-2 reduced the melting temperature to 64.3 °C, indicating restoration of the G-quadruplex structure (Supplementary Fig. 10c).

In-cell immunofluorescence analysis showed that ASO-1 reduced intracellular G4 signals in Bi-G4L-treated cells, whereas subsequent addition of ASO-2 restored G4 fluorescence (Supplementary Fig. 10d). These reversible fluorescence changes mirrored the *in vitro* observations, confirming that the ASO strategy enables reversible regulation of Bi-G4L assembly within cells. Consistently, western blot analysis demonstrated that ASO-1 restored BRD4 protein levels in Bi-G4L-treated cells, whereas subsequent addition of ASO-2 re-induced BRD4 degradation (Supplementary Fig. 10e). These results demonstrate that trivalent Bi-G4L enables reversible regulation of targeted protein degradation through ASO-controlled G4 assembly.

Tetra-G4L: a pentavalent chimera with superior degradation activity

To further enhance the BRD4 degradation capacity of G4TACs, we employed a previously reported tetramolecular G-quadruplex (Tetra-G4) scaffold. In this structure, four RNA strands provide four anchoring sites for installation of JQ1 ligands (JQ1-6mer-R) capable of binding BRD4, generating Tetra-G4 (JQ1) (Fig. 6a and Supplementary Fig. 11a) [47-49]. To recruit the E3 ligase, a well-known G4-binding ligand, tetraphenylporphyrin (TPP), was conjugated with the E3 ligand Pm, yielding an active Tetra-G4–TPP chimera (Tetra-G4L) (Fig. 6a and Supplementary Fig. 11b). To evaluate whether the TPP ligand binds Tetra-G4 with high

affinity, FRET-based fluorescence assays were performed. Cy3 and Cy5 fluorophores were used to label TPP and Tetra-G4 (Cy5-6mer-R), respectively, enabling detection of FRET signals upon formation of Tetra-G4L (Cy3–Cy5) (Supplementary Fig. 11c). Fluorescence spectroscopy revealed a strong emission peak at 670 nm upon excitation at 550 nm after addition of Cy3-TPP to Tetra-G4 (Cy5), indicating formation of the Tetra-G4L assembly with enhanced FRET signals (Supplementary Fig. 11d). Plotting fluorescence intensity at 670 nm against ligand concentration yielded a dissociation constant (K_d) of 33.8 nM, demonstrating strong binding between TPP and the Tetra-G4 scaffold (Supplementary Fig. 11e). To confirm intracellular assembly, Cy3-TPP and Tetra-G4 (Cy5) were co-introduced into cells. A strong FRET signal was detected in the ex. 550 nm–em. 670 nm channel, while no fluorescence was observed in the ex. 550 nm–em. 570 nm channel, consistent with the *in vitro* FRET results and confirming intracellular assembly of Tetra-G4L (Supplementary Fig. 11f). As a control, Cy5-labeled 5′-(UAUUUU)-3′ RNA, which a non-G-rich sequence cannot fold into a G-quadruplex, was used. In this case, strong Cy3 fluorescence was observed without detectable FRET signals, indicating that Tetra-G4L assembly depends on G4 formation (Supplementary Fig. 11f).

To optimize degradation activity, the linker connecting Pm and the TPP ligand was systematically varied. Molecular dynamics simulations revealed that the shortest distance between JQ1 and Pm (36.68 Å) was achieved when the linker contained three ethyl units (n = 3). Under this condition, the system displayed the lowest calculated energy (–12,884.76 kcal mol^{-1}) among the tested candidates (Supplementary Table 6). Subsequent molecular docking analysis further supported this configuration, providing the highest docking score (–82.72) for the n = 3 linker (Fig. 6e and Supplementary Table 7). These results collectively indicate that Pm–TPP with n = 3 provides the optimal configuration for assembling Tetra-G4L. Native gel electrophoresis showed that JQ1-6mer-RNA formed a band under Li^+ conditions, which migrated significantly slower upon addition of K^+, confirming formation of the higher-order Tetra-G4 (JQ1) structure, as K^+ is known to stabilize G-quadruplex structures more effectively than Li^+ (Supplementary Fig. 12a). Addition of Pm-TPP further increased band intensity, indicating formation of a more stable Tetra-G4L complex (Supplementary Fig. 12a). Additional structural evidence was obtained from imino proton NMR spectroscopy, which showed nearly identical proton signal patterns between Tetra-G4L and Tetra-G4L (Cy3–Cy5), confirming preservation of the G4 structure (Supplementary Fig. 12b). Circular dichroism spectroscopy further revealed enhanced positive signals at 265 nm upon titration of Pm-TPP into Tetra-G4 (JQ1) (Fig. 6b). Consistently, CD melting experiments showed an increased melting temperature of 83.6 °C for Tetra-G4L (1:1) compared with 76.1 °C for Tetra-G4 (JQ1) alone (Fig. 6c), demonstrating that Pm-TPP binding stabilizes the Tetra-G4 structure.

Prior to evaluating degradation activity, we examined whether Tetra-G4L could recruit multiple proteins. Electrophoresis analysis revealed that addition of CRBN caused the Tetra-G4L band to migrate more slowly, indicating formation of the Tetra-G4L–CRBN complex (Fig. 6d). Sequential addition of BRD4 resulted in progressively slower migration until the BRD4:Tetra-G4L ratio reached 4:1, demonstrating that Tetra-G4L can simultaneously bind four BRD4 molecules and one CRBN, forming a pentavalent G4TAC complex suitable for inducing protein degradation (Fig. 6d). Cells treated with Tetra-G4L exhibited strong G4

immunofluorescence signals, whereas almost no fluorescence was detected in cells treated with the control JQ1-5′-r(UAUUUU)-3′ a non-G-rich sequence, confirming stable intracellular formation of Tetra-G4L (Supplementary Fig. 13a).

Dose-dependent experiments demonstrated that Tetra-G4L efficiently induced BRD4 degradation (Fig. 6f, 6g and 6h). The calculated DC_{50} was 0.42 nM, which is lower than those observed for Bi-G4 and Bi-G4L (Fig. 6g and Supplementary Fig. 6c). This enhanced activity is likely attributable to the higher binding valency and improved physiological stability of Tetra-G4L (Supplementary Fig. 2c). In contrast, a control system comprising JQ1-5′-(UAUUUU)-3′ and Pm-TPP failed to induce BRD4 degradation even at concentrations up to 100 nM (Supplementary Fig. 13b). Time-course western blot analysis revealed substantial BRD4 degradation as early as 4 h after Tetra-G4L treatment (Supplementary Fig. 13c). The degradation effect persisted for 48–72 h, comparable to the preclinical PROTAC ARV-825, which suppresses BRD4 levels for more than 24 h after treatment (Fig. 6h) [50,51]. Furthermore, when an additional dose of Tetra-G4L was administered at 72 h, BRD4 degradation was maintained, with no significant recovery observed even after 120 h (Fig. 6h). Collectively, these results demonstrate that Tetra-G4L acts as a potent and durable protein degrader capable of efficiently suppressing BRD4 levels in cells, highlighting its potential for targeting cancers characterized by BRD4 overexpression.

G4TACs inhibit cancer cell proliferation and reduce cell viability

We next investigated whether G4TAC-mediated BRD4 degradation suppresses cancer cell growth. Western blot analysis revealed increased apoptotic responses in cells treated with Bi-G4, Bi-G4L, and Tetra-G4L, as evidenced by elevated levels of cleaved caspase-3 accompanied by BRD4 degradation (Fig. 7a). In contrast, the control components Bi-G4 (JQ1) and Pm-7OTD, which do not induce BRD4 degradation, produced only minimal apoptotic responses (Fig. 7a). Clonogenic assays further demonstrated that Bi-G4 significantly inhibited cell proliferation, with an IC_{50} value of 52.7 nM (Fig. 7d and Supplementary Fig. 14a). Stronger antiproliferative effects were observed in cells treated with Bi-G4L and Tetra-G4L, which exhibited IC_{50} values of 20.5 and 15.8 nM, respectively (Fig. 7b–d). These results are consistent with the protein degradation data, indicating that increasing binding valency enhances the biological activity of G4TACs. Bi-G4 (JQ1) alone also showed moderate inhibitory activity (IC_{50} = 156.4 nM), likely because JQ1 functions as a stable BRD4 inhibitor (Fig. 7d and Supplementary Fig. 14b). In contrast, Pm-7OTD alone did not exhibit significant inhibitory effects, even at concentrations up to 2 μM (Fig. 7d and Supplementary Fig. 14c).

To determine whether ASO regulation could modulate the cytotoxicity of G4TACs, ASO switching experiments were performed. Addition of ASO-1 rescued the proliferation inhibition induced by Bi-G4 (Supplementary Fig. 15). Subsequent addition of ASO-2 restored the inhibitory effect, reducing cell proliferation to levels comparable to Bi-G4 treatment after 72 h (Supplementary Fig. 15). Importantly, treatment with ASO-2 alone did not affect cell proliferation, excluding potential off-target effects (Supplementary Fig. 15). Similar results were observed for ASO-regulated Bi-G4L assembly (Supplementary Fig. 16). These findings demonstrate that ASO–G4TACs coupling enables programmable control of cytotoxicity

through reversible protein degradation, potentially mitigating the on-target toxicity associated with conventional PROTAC therapies.

Cell viability was further evaluated using live/dead staining assays. Treatment with Bi-G4, Bi-G4L, and Tetra-G4L induced significant cell death, as indicated by increased propidium iodide (PI) staining of dead cells and decreased calcein-AM fluorescence in living cells. The corresponding LC_{50} values were 68.1, 23.9, and 18.3 nM, respectively (Fig. 7e–g and Supplementary Fig. 17). Bi-G4 (JQ1) also induced cell death but with a weaker effect (LC_{50} = 428.2 nM) (Fig. 7g and Supplementary Fig. 17b). In contrast, cells remained largely viable when treated with Pm-7OTD even at 2 μM (Fig. 7g and Supplementary Fig. 17c). Collectively, these results suggest that G4TACs exhibit potent anticancer activity *in vitro*.

G4TACs suppress adrenocortical carcinoma growth *in vivo*

To evaluate the therapeutic potential of G4TACs *in vivo*, we established an adrenocortical carcinoma (ACC) xenograft mouse model. SW-13 cells were implanted into female BALB/c nude mice, and treatment was initiated 9 days after implantation. G4TACs were administered every three days for eight cycles, and tumor progression was monitored over 21 days (Fig. 8a). Tumor volume measurements revealed that G4TAC treatment significantly suppressed tumor growth compared with the PBS control group (Fig. 8b and 8c). Importantly, no significant body weight changes were observed during treatment, indicating low systemic toxicity (Supplementary Fig. 18). Western blot analysis of tumor lysates confirmed efficient BRD4 degradation and induction of apoptosis in tumor tissues following G4TAC treatment (Fig. 8d). Consistently, H&E staining revealed marked morphological changes and reduced tumor cell density in treated tumors compared with controls (Fig. 8e). Together, these results demonstrate that G4TAC-mediated BRD4 degradation induces robust antitumor activity *in vivo*, highlighting the potential of this strategy for targeted cancer therapy.

G4TACs function as a universal platform for targeted protein degradation

To explore whether G4TACs could serve as a versatile protein degradation platform, we next targeted anaplastic lymphoma kinase (ALK) using the FDA-approved kinase inhibitor ceritinib as the warhead. Ceritinib could block both native and mutant ALK and has been widely used for the treatment of non-small-cell lung cancer (NSCLC) since its approval in 2014 (Fig. 9a and 9b). To construct ceritinib-based G4TACs, ceritinib was conjugated to RNA through a previously reported ethylene glycol linker, generating CER-6 mer-R for assembly of Tetra-G4L (CER) (Fig. 9c). Molecular dynamics simulations indicated that the optimal configuration was achieved when the ethylene glycol linker contained two units (n = 2), resulting in a ceritinib–Pm distance of 39.98 Å and the lowest calculated energy (–13,934.82 kcal mol^{-1}) among tested candidates (Supplementary Table 8). Molecular docking analysis further supported this design, providing a high docking score (–74.97) (Fig. 9d and Supplementary Table 9). Imino proton NMR spectroscopy revealed characteristic G4 imino proton signals (10–12 ppm) for Tetra-G4L (CER), confirming that ceritinib modification does not disrupt the G-quadruplex structure (Supplementary Fig. 19a).

To evaluate ALK degradation, Tetra-G4L (CER) was introduced into TK-ALCL1 cells (Fig. 9e and Fig. 9f). Western blot analysis showed that NPM–ALK protein levels decreased in a dose-dependent manner, yielding a DC_{50} value of 2.81 nM, which is lower than

previously reported ceritinib-based PROTAC systems (10 nM) (Fig. 9f and Supplementary Fig. 6d). As a control, a non-G-rich sequence (ceritinib-5′-r(UAUUUU)-3′) incapable of forming G4 structures was used. NMR analysis confirmed the absence of G4 imino signals, indicating disruption of the G-quadruplex scaffold (Supplementary Fig. 19b). Correspondingly, no ALK degradation was observed even at RNA concentrations up to 1000 nM (Supplementary Fig. 19c). These results demonstrate that the G4TACs strategy can accommodate FDA-approved ligands such as ceritinib to enable efficient degradation of alternative targets, highlighting the potential of G4TACs as a universal platform for targeted protein degradation.

Discussion

This study presents a modular platform for controllable protein degradation based on non-covalent G-quadruplex (G4) assemblies, extending the PROTAC concept to nucleic acid–engineered frameworks. In this strategy, intermolecular G4 scaffolds and G4–ligand conjugates were designed to assemble functional G4TAC complexes, in which both target-binding ligands and E3 ligase binders can be incorporated. G-quadruplex structures have been widely explored as bioengineering materials due to their high stability, structural programmability, and compatibility with biological environments[52,53], enabling the formation of active G4TAC assemblies inside cells and subsequent protein degradation.

As a programmable platform, G4TACs exhibit several advantages over conventional PROTAC systems. First, the assemblies form under physiological conditions without requiring additional chemical or photochemical stimuli, thereby avoiding the cytotoxicity commonly associated with photo-responsive or chemically activated degradation strategies[39,54]. Second, the structural diversity of G4 conformations and ligand-binding modes enables a “LEGO-like” design principle, allowing ligands and E3 binders to be positioned in multiple spatial orientations. This modular architecture facilitates optimization of degradation efficiency by tuning the distance and geometry between functional components.

Multivalent PROTAC strategies have previously been proposed to enhance degradation efficiency, but increasing valency often leads to poor solubility and synthetic complexity[55]. G4TACs address these limitations by exploiting oligonucleotide scaffolds, which are inherently water soluble and readily synthesized through standard solid-phase methods. Using this approach, we constructed bi-, tri-, and higher-valent assemblies, which exhibited progressively enhanced degradation activity. Compared with conventional PROTAC molecules that require multiple organic synthesis steps, oligonucleotide-based platforms offer a simpler and potentially more scalable route toward therapeutic development.

Another key feature of this system is its reversible regulatory capability. This advantage distinguishes it from aptamer–PROTAC conjugates[56], which generally lack reversible control and are typically limited to degrading DNA- or RNA-binding proteins[57-59], as reported in our previous study[60]. Controllable protein degradation has attracted increasing interest for precision therapies aimed at reducing adverse effects arising from uncontrolled target depletion[61]. Previously reported switchable PROTAC systems, including click-to-release reactions, radiation-induced decaging, and enzyme-triggered activation, primarily operate through irreversible “off-to-on” activation mechanisms[36,40]. In contrast, the integration of antisense oligonucleotide (ASO) regulation with G4TAC assemblies enables reversible switching of protein degradation, allowing dynamic control of protein levels in cells. Such a

reversible system provides a potential strategy to balance therapeutic efficacy with safety by enabling spatiotemporal regulation of degradation activity.

In this work, G4TACs were initially demonstrated using JQ1-mediated targeting of BRD4, resulting in efficient degradation and potent anticancer activity. To further examine the versatility of this platform, we incorporated the FDA-approved ALK inhibitor ceritinib, which enabled robust degradation of NPM–ALK in lymphoma cells. These results indicate that G4TACs can accommodate clinically relevant ligands and may serve as a general framework for targeting diverse disease-associated proteins.

The modularity of G4TACs also allows extensive future expansion. For example, different E3 ligase ligands, such as CRBN, VHL, or MDM2 binders, could be incorporated into the G4 framework to diversify degradation pathways (Fig. 10a). Moreover, a single G4 scaffold could potentially integrate multiple target-binding ligands, enabling simultaneous degradation of several proteins for investigating complex signaling networks or implementing combinatorial therapeutic strategies. Beyond small-molecule ligands, DNA/RNA aptamers or peptide-based binders may also be incorporated as targeting elements, which warrants further exploration in future studies (Fig. 10b,c). For potential clinical translation, efficient delivery strategies will be essential. Receptor-targeted lipid nanoparticle systems, which have demonstrated strong performance in nucleic acid delivery, may provide a viable route for delivering G4TACs into tumor tissues and improving therapeutic efficacy[11,62].

In summary, this work establishes G4TACs as a programmable and versatile platform for targeted protein degradation, combining multivalent target engagement, reversible regulatory capability, and robust anticancer activity. These findings expand the conceptual framework of PROTAC technologies and provide a foundation for developing next-generation degraders based on higher-order nucleic acid structures.

Methods

Chemical synthesis

Details of the synthesizing the small molecular compounds are provided in the Supplementary data (Supplementary Schemes 1–8 and Supplementary Fig. 20–64). All chemical NMR analyses were processed with TopSpin 3.0 (Bruker BioSpin Gmbh) software and analyzed by MestReNova (v14.0.0).

DNA or RNA synthesis

By using an automatic solid-phase phosphoramidite chemistry and DNA/RNA synthesizer, designed DNAs or RNAs were synthesized at a ratio of 1.0 μmol. Following the oligonucleotides were cleavage from CPG and deprotected by using AMA (Ammonium Hydroxide/40% aqueous methylamine 1:1 v/v) at room temperature for 20 min and at 65 °C for 10 min, respectively. TBDMS protections were removed by treatment with triethylamine trihydrofluoride followed by filtration through an ion exchange cartridge (RNA only). The oligomers were further purified by HPLC in a linear gradient of 50 mM ammonium formate in 1:1 acetonitrile/H_2O and 50 mM ammonium formate in H_2O. The oligomers were desalted through a NAP 10 column (GE Healthcare) and identified by MALDI-TOF-MS on an

Autoflex III smart beam mass spectrometer (Supplementary Fig. 65–81). Concentrations of oligonucleotides were defined using a Nanodrop one spectrophotometer before use.

Design and structural determination of G4TACs

Heterobifunctional Bi-G4 model comprising 6 and 16 mer DNAs (5'-TAGGGT-3'/5'-GGGTTAGGGTTAGGGT-3') was directly obtained from the Protein Data Bank (PDB) (code: 2AQY). ^{F}G residues were incorporated into the positions including G3 of 6 mer DNA and G1, G7, G8 and G13 of 16 mer DNA to stabilize the G4 structure. Next, JQ1 and Pm ligands were manually ligated onto the 5'-end of 16 and 6 mer DNA by a series of designed aliphatic linker with varying lengths. All models were subjected to geometry clean, solvation and energy minimization at 10^4 times under the physiological condition (BIOVIA Discovery Studio 4.5; 37°C, 100 mM KCl). Every model with identical linker provided 30 thermodynamic conformations and the final one with lowest energy was defined. The CHARMM energy and the distance between JQ1 and Pm of each screened model were evaluated and the results were shown in Supplementary Table 2.

In order to construct trivalent Bi-G4L assembly, the G4–7OTD conjugate model was obtained from PDB (code: 2MB3). Similarly, ^{F}G residues were incorporated into the above targeted positions as well as two JQ1 ligands were introduced onto the 5'-end of 16 and 6 mer DNA with identical linker (methylene numbers, n = 3) which indicated lowest energy when used to conduct Bi-G4 model. Afterwards, Pm was connected to 7OTD through designed linker with varying length. These assemblies were subjected to geometry clean, solvation and energy minimization at 10^4 times under the physiological condition (BIOVIA Discovery Studio 4.5). The model with lowest energy screening from total 30 conformations of every conjugate was defined. The CHARMM energy and the distance between JQ1 and Pm of each screened model were evaluated and the results were shown in Supplementary Table 4.

For conducting Tetra-G4L assembly, the NMR-restrained Tetra-G4 (RNA sequence: 5'-UAGGGU-3') was used based on our previous report[63]. JQ1 molecules were ligated onto the 5'-end of all four oligonucleotides with the identical linker (methylene numbers, n = 3) as above determined. The resulted Tetra-G4 (JQ1) was bounded to a series of Pm-TPP conjugates with varying linker by following a reported method[47,48], where provide a prefabricated Tetra-G4L assembly. Next, a set of molecular dynamic simulation processes containing solvation, heating (denature), cooling (renature) and equivalence were carried out, producing 30 conformers of every assembly with individual linker and the conformer with lowest energy was defined (BIOVIA Discovery Studio 4.5). The CHARMM energy and the distance between JQ1 and Pm of each screened model were evaluated and the results were concluded in Supplementary Table 6. Following the identical process as above, Tetra-G4L (CER) assembly was conducted, corresponding CHARMM energy and the distance between ceritinib and Pm of each screened model were evaluated and the results were concluded in Supplementary Table 8.

Molecular docking analysis

The molecular docking studies of G4TACs with BRD4 and CRBN proteins were performed using BIOVIA Discovery Studio 4.5. The crystal structures of BRD4 and CRBN proteins were downloaded from PDB (code: 6BOY). For the G4TACs with BRD4 docking, the readily

prepared PDB models of G4TACs were used. Prior to docking, the protein underwent preprocessing using QuickPrep with default options, which included rectifying structural inaccuracies, incorporating hydrogen atoms, optimizing three-dimensional H-bonding networks, eliminating water molecules beyond 4.5 Å from the protein, and minimizing within a limited range of 8 Å of the altered base pairs. Next, JQ1 molecule was defined as ligand pose and docking boxes were generated around the site. The native ligand pockets of the BRD4 protein were selected as the receptor site in the docking studies. The Discovery Studio module was then used to dock G4-loaded JQ1 into the binding site of BRD4 using a conventional protocol, which generated several docking poses based on the predicted interaction energies between the ligand and receptor[15]. The docking poses were ranked according to their binding affinities, and their docking score was recorded. The pose with the highest docking score was selected as the final result (Supplementary Tables 3, 5, 7). The docking score was calculated according to a reported method[15].

In addition, the molecular docking studies of Tetra-G4L (CER) with ALK and CRBN proteins were performed using BIOVIA Discovery Studio 4.5. The crystal structures of ALK and CRBN proteins were downloaded from PDB (code: 4MKC). For the G4TACs and ALK docking, the readily prepared PDB models of G4TACs were used. Docking experiment followings above method and the results shown in Supplementary Table 9.

Similarly, for studying G4-loaded Pm with CRBN docking, above principles was used to carry out the docking experiments. Consequently, docking poses were produced and ranked according to their binding affinities, and their docking scores were recorded. The pose with the highest docking score was selected as the final result (Supplementary Tables 3, 5, 7, 9).

^{1}H NMR experiments

For spectra recorded in 90% H_2O/10% D_2O water signal was suppressed using the 3–9–19 WATER-GATE pulse sequence or excitation sculpting with gradient pulse. The data were processed with TopSpin 3.0 (Bruker BioSpin Gmbh) software and analyzed with MestReNova software. For 1D NMR measurement, G4TACs samples of 1 mM concentration were dissolved in 150 μL of designed solution containing 10% D_2O, 100 mM KCl and 25 mM K-PO_4 buffer (pH 7.0). Samples were prepared by heating the oligonucleotides at 85 °C for 3 min and gradually cooling to room temperature before use.

CD spectrum

CD experiments were performed by using a JASCO model J-820 CD spectrophotometer (JASCO Corporation, Tokyo, Japan). Condition: 20 μM G4TACs samples in 100 mM KCl and 25 mM K-PO_4 buffer (pH 7.0) at 10°C. For studying reversible controlled G4TACs structure, 20 μM ASO-1 and ASO-2 were alternatively added into the DNA solution with a interval time of 5 min following measurements with each treatment. The melting curves were obtained by monitoring at 260, 265 or 290 nm according to different DNA or RNA conformations, 20 μM G4TACs in 0.3 mL samples containing 100 mM KCl and 25 mM K-PO_4 buffer (pH 7.0). 20 μM ASO-1 was added into above G4TACs solution when studying reversible controlled G4TACs structure.

Native gel electrophoresis

For studying the G4 or G4–ligand conjugate formation, 1 μM of DNA, RNA (single strand concentration) or ligand was dissolved in the 20 μL of solution containing 100 mM KCl, 25 mM $MgCl_2$ and 25 mM K-PO_4 buffer (pH 7.0). Each sample was treated with heat denaturation, renaturation and was stored at 25 °C at least for 12 h. Then 3 μL of 30% glycerol was added before loading onto gel. Native gel electrophoresis (PAGE) was run on 20% polyacrylamide gel (acrylamide/bisacrylamide, 29:1) at 4 °C, in 1 × TBE buffer. To study the G4TACs bounding BRD4 (MedChemExpress, recombinant protrin, 54 kDa) or CRBN (MedChemExpress, recombinant protrin, 56 kDa), readily prepared 1 μM of G4TACs was mixed with protein at requisite ratios in the 20 μL of solution containing 100 mM KCl, 25 mM $MgCl_2$, 1 mM EDTA and 25 mM K-PO_4 buffer (pH 7.0). The sample was kept at 4 °C overnight before use. Native PAGE was run on 12% polyacrylamide gel (acrylamide/bisacrylamide, 29:1) at 4 °C, in 1 × TBE buffer. The DNA, RNA and DNA ladder (TaKaRa Bio.) were stained with gelstar (Lonza) by dilution with 1:1000 in running buffer and visualized at Alexa fluor 488 channel with ex. 480 nm and em. 520 nm using a phosphorimager (LAS-4000, Fujifilm).

Binding affinity assay between Tetra-G4 and TPP ligand

20 nM Cy3-labeled Tetra-G4 in presence of 50 mM Tris-HCl, pH 7.0, 100 mM KCl and 10 mM $MgCl_2$ was titrated by Cy5-TPP ligand with concentration dependent. The fluorescence spectrum was monitored by using a fluorescence spectrophotometer (FP-8200, Jasco, Japan). The experiment was carried out by exciting at 530 nm and the fluorescence intensity at 670 nm was recorded under each conditions. Finally, the concentrations of Cy5-TPP ligand and corresponding fluorescence intensity at 670 nm was fitted into a non-liner analysis. A dissociation constant (K_d) could be calculated by the following equation, $F = F_{max} \times [protein]/K_d + [protein]$, where F is the relative fluorescence intensity, and F_{max} is its maximum value.

G4TACs and proteins binding assay

The Human recombinant BRD4 (O60885-1) and CRBN (M1-L442) proteins were purchased from MedChemExpress. Fluorescence titrations were performed to determine the equilibrium dissociation constant (K_d) of G4TACs with proteins. The Cy3 dye was used to label G4TACs for providing fluorescence response upon binding event, which was excited at 550 nm and the emitted at 570 nm. Fluorimetric titration experiments were performed on a fluorescence spectrophotometer (FP-8200, Jasco, Japan). A constant amount of G4TACs assembly (100 nM) was titrated against increasing concentration of BRD4 (0 − 400 nM) or CRBN (0 − 1600 nM) in the buffer (50 mM Tris-HCl, pH 7.0, 100 mM KCl, 10 mM $MgCl_2$, 5 mM DTT and 1 mM EDTA) at 25 °C. For the competitive assay, 100 nM G4TACs was mixed to 100 nM JQ1 or Pm before titration experiment beginning. A control experiment was carried out in identical conditions with the presence of the unlabeled G4TACs (100 nM) and increasing amounts of the proteins. The fluorescence changes from the control experiments were subtracted from the data obtained with the Cy3 labeled G4TACs, and the corrected values were plotted against the corresponding protein concentration. The dissociation constant K_d was calculated using the following equation, $F = F_{max} \times [protein]/K_d + [protein]$, where F is the relative fluorescence intensity, and F_{max} is its maximum value.

In-cell G4TACs assembly by oligonucleotides

200 nM single strand DNA or ligand were incorporated into HeLa cells (5×10^4) with Lipofectamine 3000 transfection. The treated cells were incubated for 6 h and washed twice with PBS buffer. Next, complementary oligonucleotides (assembling into G4) or Bi-G4 (JQ1) were subjected to cells by transfection and kept for 3 h before the fluorescence quantitative assay of G4 by immunofluorescence staining. For studying the in-cell G4TACs assembly induced BRD4 degradation, 2×10^6 HeLa cells were used and treated by 1 μM single strand DNA or ligand by transfection. The treated cells were incubated for 2 h and washed twice with PBS buffer. Next, complementary oligonucleotides (assembling into G4) or Bi-G4 (JQ1) were subjected to cells by transfection and kept for 24 h before the quantitative assay of BRD4 protein using western blotting.

G4TACs physiological stability assay

100 μL RIPA buffer with 10 μL fresh protease/phosphatase inhibitors was added into the HeLa cells (1×10^7). Adherent cells were scraped off and resuspended in buffer and keep on ice with agitation for 20 min. The obtained suspension was spin at 4 °C with 12,000 rpm for 20 min to pellet cell debris. Next, the supernatant was collected and mixed with PBS buffer (pH 7.0) to get a 10% cell lysate solution. Prepared G4TACs or other oligonucleotides were added into above cell lysate at 20 μL followed by mixing 3 μL of 30% glycerol before loading onto gel. Native gel electrophoresis (PAGE) was run on 20% polyacrylamide gel (acrylamide/bisacrylamide, 29:1) at rt, in 1 × TBE buffer. The nucleic acid molecules were stained by gelstar (Lonza) and visualized at a fluorescence channel with ex. 480 nm and em. 520 nm using a phosphorimager (LAS-3000, Fujifilm).

Cell culture

Human HeLa (CCL2), SW-13 (CCL-105) cells grown in Dulbecco's modified Eagle's medium (DMEM) containing 10% FBS under a 5% CO_2 atmosphere were harvested at numbers and washed twice before use. TK-ALCL1 (CVCL_E2T4) cells maintained in Roswell Park Memorial Institute (RPMI) 1640 medium (Fujifilm, Wako, Osaka, Japan) supplemented with 10% heat-inactivated fetal bovine serum (FBS) (Sigma-Aldrich, St. Louis, MO, USA), 5% of sterile-filtered 100 mM of L-sodium pyruvate solution (Nacalai Tesque, Kyoto, Japan), streptomycin (100 μg/ml), and penicillin (100 U/ml) in an incubator at 37 °C, 5% CO_2. The culture medium was changed every 3–4 days. The cells were harvested at numbers and washed twice before use.

Immunofluorescence staining

G4TACs were transfected into live HeLa cells (5×10^4) by transportation with Lipofectamine 3000 (Thermo Fisher Scientific) according to the manufacturer's protocol in a final concentration of 200 nM. The treated cells were washed by PBS buffer and fixed with 4% paraformaldehyde. Thereafter, these cells were permeabilized with 0.2% Triton X-100 and subjected to primary antibody, 5 μL G-quadruplex antibody BG4 (Sigma-Aldrich) with 1:100 dilution at 37°C for 1 h. After three washes in PBS, slides were incubated with 10 μL anti-FLAG antibody (1:800 dilution) (#8146, Cell Signaling Technology) at 4°C for overnight,

and then incubated with (Alexa Fluor® 488 antibody (1:500 dilution) (ab150105, Abcam) at 37°C for 1 h. Following an additional three washes in PBS, slides were imaged by confocal microscopy on a Olympus confocal microscopy (Evident Scientific, FV4000). The data were recorded using Olympus software. The laser of Olympus 60 × oil objective, X-Apo, 1.42NA/0.15WD. The green fluorescence for Alexa fluor 488 dye was an excitation wavelength of 488 nm. The excitation/emission filter of 480 − 490nm/495 − 520 nm was used. The red fluorescence for Cy3 dye was an excitation wavelength of 550 nm. The excitation/emission filter of 520 − 550 nm/550 − 600 nm was used. For the FRET assay in cells, a combination at Cy3-excitation filter of 520 − 550 nm and Cy5-emission filter of 650 − 700 nm was used.

Western blotting (WB)

HeLa cells were seeded at a density of 2×10^6 cells/well in every dish (35×35 mm^2) and allowed to adhere and grow overnight. G4TACs were transfected into live cells by transportation with Lipofectamine 3000 (Thermo Fisher Scientific) according to the manufacturer's protocol with requisite experimental conditions. Notably, Pm-ligand was used at consistent 2 μM to promise it's bounding to G4 in cells. The cells were then co-incubated for predefined times at 37 °C in an incubator. After the incubation period, the cells were collected and subjected to WB analysis. Next, the cells were collected by centrifugation, washed with ice-cold PBS three times, and lysed with RIPA lysis buffer (RIPA:PMSF = 99:1) for 20 min on ice. The lysates were centrifuged at 14,000g for 15 min at 4 °C. The protein concentration of the supernatants was measured using a Nanodrop one spectrophotometer. The protein extract was mixed with dual-color protein loading buffer, denatured in a 100 °C bath for 10 min, and loaded onto an SDS–PAGE gel. The proteins were then transferred to a PVDF membrane by electrophoresis. After blocking non-specific binding sites with 5% BSA in 1 × TBST, the membrane was incubated with the appropriate primary antibody mouse anti-BRD4 antibody (Catalog No. Ag27545, Proteintech) and rabbit anti-β-actin antibody (Catalog No. 20536-1-AP, Proteintech) at 4 °C overnight. Following three washing steps of 10 min each with 1 × TBST, the membrane was incubated with a matched HRP conjugated secondary antibody HRP-conjugated goat anti-rabbit IgG antibody (Catalog No. SA00001-2, Proteintechand) and HRP-conjugated goat anti-mouse IgG antibody (Catalog No. SA00001-1, Proteintech) at room temperature for 1.5 h, followed by another three washing steps. After adding HRP chromogenic substrate, the signal was detected by chemiluminescence on a FUSION Gel Imaging System (M&S instrument Inc.). The protein levels were quantified by the gray values of bands in the resulting images using ImageJ (Wayne Rasband, NIH, USA).

Protein degrading pathway assay

Prepared 2×10^6 HeLa cells were treated by 20 μM small molecule including JQ1, Pm or MG132 respectively before 1 μM G4TACs transfection. The cells were then co-incubated for 24 h at 37 °C in an incubator. Next, cells were collected and subjected to WB analysis following the standard process as above description.

Reversible switching G4TACs with fluorescence assay

The Cy3- and Cy5-labeled Bi-G4 at 200 nM concentration was dissolved in a buffer of 50 mM Tris-HCl, pH 7.0, 100 mM KCl and 10 mM $MgCl_2$ at 25 °C. Fluorescence excitation-emission assay was conducted using a fluorescence spectrophotometer (FP-8200, Jasco, Japan). The sample was excited at 530 nm and emission spectrum was monitored at 550-700 nm. Next, 1 μM ASO-1 and ASO-2 were alternatively added into above solution with a interval time of 5 min, the corresponding fluorescence emission data was recorded at each experiments.

Fluorescence imaging of reversible controllable G4TACs *in vitro*

The 200 nM Cy3- and Cy5-labeled Bi-G4 in the presence of 50 mM Tris-HCl, pH 7.0, 100 mM KCl and 10 mM $MgCl_2$ were incubated at 25 °C. Fluorescence imaging *in vitro* was performed using an imaging system (Lumazone CMS, Shoshin EM,Japan). The experiment was carried out by alternatively adding 1 μM ASO-1 and ASO-2 into above solution with a interval time of 5 min, the corresponding fluorescence image was recorded at each experiments. A Cy3-channel with a filter of filter of ex. 520 − 550 nm/570 − 600 nm was used following ASO-1 treatment, indicating green color. The FRET channel of ex. 520 − 550 nm/660 − 780 nm was used to monitor the fluorescence after ASO-2 treatment or Bi-G4 alone, presenting red color.

Reversible switching ternary complex of Bi-G4 with proteins

1 μM of G4TACs in presence of 1 μM BRD4 and CRBN in the 20 μL of solution containing 100 mM KCl, 25 mM $MgCl_2$, 1 mM EDTA and 25 mM K-PO_4 buffer (pH 7.0), was kept at 4 °C overnight before use, Afterward, 5 μM ASO-1 and ASO-2 were alternatively added into above solution with a interval time of 1 h at 4 °C. Every individual experiments were used to carry out the native PAGE assay using 12% polyacrylamide gel (acrylamide/bisacrylamide, 29:1) at 4 °C, in 1 × TBE buffer. The oligonucleotides were stained with gelstar (Lonza) by dilution with 1:1000 in running buffer and visualized at Alexa fluor 488 channel with ex. 480 nm and em. 520 nm using a phosphorimager (LAS-4000, Fujifilm).

Reversible switching G4TACs formation in cells

200 nM G4TACs was introduced into 5×10^4 HeLa cells by a transfection protocol. Next, 1 μM ASO-1 and ASO-2 were alternatively added into above solution with a interval time of 1 h at 37 °C. Every treatment was used to carry out a immunofluorescence staining assay to quantitatively calculate the G4 intensity through using the standard protocol of BG4 antibody use. Cell slides were imaged by confocal microscopy on a Olympus confocal microscopy (Evident Scientific, FV4000). The data were recorded using Olympus software.

Reversible switching G4TACs degrades BRD4

G4TACs of 1 μM concentration was introduced into 2×10^6 HeLa cells by a Lipofectamine 3000 transfection method and the cells were incubated for 16 h at 37 °C. Next, 5 μM ASO-1 and ASO-2 were alternatively added into cell dishes with a interval time of 16 h. Every treatment was used to carry out the WB analysis following the standard process as above description for quantitatively calculating the BRD4 contents. The results were detected by chemiluminescence on a FUSION Gel Imaging System (M&S instrument Inc.). The protein

levels were quantified by the gray values of bands in the resulting images using ImageJ (Wayne Rasband, NIH, USA).

Cell apoptosis assay

The HeLa cells (2×10^6) were seeded into the dish of 35×35 mm^2 and incubated overnight. After 24 h of seeding, the G4TACs or control groups were added with Lipofectamine 3000 (Thermo Fisher Scientific) transfection according to the manufacturer's protocol with requisite experimental conditions, and the cells were incubated for another 16 h. The cells were then co-incubated for predefined times at 37 °C in an incubator. After the incubation period, the cells were collected and subjected to WB analysis. Next, the cells were collected by centrifugation, washed with ice-cold PBS three times, and lysed with RIPA lysis buffer (RIPA:PMSF = 99:1) for 20 min on ice. The lysates were centrifuged at 14,000g for 15 min at 4 °C. The protein concentration of the supernatants was measured using a Nanodrop one spectrophotometer. The protein extract was mixed with dual-color protein loading buffer, denatured in a 100 °C bath for 10 min, and loaded onto an SDS–PAGE gel. The proteins were then transferred to a PVDF membrane by electrophoresis. After blocking non-specific binding sites with 5% BSA in 1 × TBST, the membrane was incubated with the appropriate primary antibody rabbit anti-cleaved caspase-3 antibody (Catalog No. 9661T, Cell Signaling Technology, Inc.) at 4 °C overnight. Following three washing steps of 10 min each with 1 × TBST, the membrane was incubated with a matched HRP conjugated secondary antibody HRP-conjugated goat anti-rabbit IgG antibody (Catalog No. SA00001-2, Proteintechand) at room temperature for 1.5 h, followed by another three washing steps. After adding HRP chromogenic substrate, the signal was detected by chemiluminescence on a FUSION Gel Imaging System (M&S instrument Inc.). The protein levels were quantified by the gray values of bands in the resulting images using ImageJ (Wayne Rasband, NIH, USA).

Cell clonogenicity assay

The HeLa cells (2×10^4) were cultured as description above. The G4TACs or control groups were transfected into living HeLa cells by transportation with Lipofectamine 3000 (Thermo Fisher Scientific) according to the manufacturer's protocol. Notably, Pm-ligand was used at consistent 2 μM to promise it's bounding to G4 in cells.

The cells then were imaged in bright-field after 72 h and the cell colonies were stained for 20 min in 4% (w/v) methylene blue solution in PBS and washed. Colonies were counted and plotted as percentage of PBS-treated control. In each group experiments, three independent experiments were completed and three images obtained in each result, one representative image that was randomly selected from the totally obtained three confocal images and defined as presentation.

Cell viability assay

In this study, HeLa cells grown in Dulbecco's modified Eagle's medium (DMEM) medium containing 10% FBS under a 5% CO_2 atmosphere were harvested (2×10^4) and washed twice by using Hanks' Balanced Salt Solution (HBSS) buffer before use. G4TACs were transfected into live HeLa cells by transportation with Lipofectamine 3000 (Thermo Fisher Scientific) according to the manufacturer's protocol. Notably, Pm-ligand was used at consistent 2 μM to

promise it's bounding to G4 in cells. After that, the cells were imaged in bright-field after 72 h. Next, the nuclear DNA in dead and live cells were stained by PI (Dojindo) and calcein-AM (Dojindo). The cells were incubated with PI or calcein AM in PBS (1.0 μM) for 20 min at 37 °C. The excitation and the absorbance filter was 550/12 nm and 600/40 nm for PI, or 488/40 and 530/30 for calcein-AM. Cell viability study was represented by the cells with green fluorescence (normalized by the green fluorescence of calcein staining from the PBS treated cells sample). In each group experiments, three independent experiments were completed and >10 images obtained in each result. At least 5 images that were randomly selected from the totally obtained confocal images >10 pieces containing intact cells, in which the representative images was divided into at least 4 subunits with equal size and the most representative one finally defined as presentation.

Xenograft Mouse Model and Drug Treatment

BALB/c nude mice (aged 6 weeks) were purchased from Charles River Laboratories Japan (Yokohama, Japan). Mouses were housed in pathogen-free conditions with standard temperature and humidity at the Laboratory Animal Resources Center of University of Miyazaki. All the animal experiments were approved by the Institutional Animal Care and Use Committee of University of Miyazaki. The anti-tumor performance of G4TACs was evaluated in SW-13 adrenocortical carcinoma xenograft model *in vivo*. The female Balb/c nude mice were s.c. injected with 100 μL of cell suspension (1×10^7 cells). The tumor volume reached 100 mm^3 at 9-days post inoculation. The tumor-bearing mice were randomly grouped (n = 3), and treated with different drugs for 8 cycles at a time interval of 3 days. **Group 1:** s.c. injected with 10 mg/kg dose of Bi-G4L coated with *in vivo*-jetDNA® *in vivo* DNA transfection reagent (Catalog No. SL100499, SignaGen Laboratories). **Group 2:** s.c. injected with 10 mg/kg dose of Tetra-G4L coated with *in vivo*-jetDNA® *in vivo* DNA transfection reagent (Catalog No. SL100499, SignaGen Laboratories). **Group 3:** s.c. injected with saline coated with *in vivo*-jetDNA® *in vivo* DNA transfection reagent (Catalog No. SL100499, SignaGen Laboratories). The tumor volume and body weights of the animals were monitored during the whole experimental period. All tumors were harvested at the end of the antitumor studies, and examined by H&E. BRD4 degradation in the tumor tissue was validated by western-blotting of the tumor lysate.

Statistics and Reproducibility

The quantitative analyzing results are presented as the mean ± standard deviation (SD) generated by GraphPad Prism (version 10, GraphPad Software Inc., USA). Each experiment was independently repeated three or five times. The data analysis was conducted by using Origin software (Version 2024, OriginLab Software Inc., USA).

Reporting summary

Further information on research design is available in the Nature Portfolio Reporting Summary linked to this article.

Data availability

All data generated in this study are provided in the Supplementary Information and Source Data file. All molecular docking models of G4TACs–proteins were uploaded onto the ModelArchive, including BRD4–Bi-G4–CRBN (accession code: ma-3xyof), BRD4–Bi-G4L–CRBN (accession code: ma-sc6cu), BRD4–Tetra-G4L–CRBN (accession code: ma-yl0il) and ALK–Tetra-G4L (CER)–CRBN (accession code: ma-l8dux). Source data are provided in this paper.

References

1. Li, H. *et al.* Protein degradation technology: a strategic paradigm shift in drug discovery. *J. Hematol. Oncol.* **14**, 138 (2021).
2. Burslem, G. M. & Crews, C. M. Proteolysis-targeting chimeras as therapeutics and tools for biological discovery. *Cell* **181**, 102-114 (2020).
3. Schapira, M., Calabrese, M. F., Bullock, A. N. & Crews, C. M. Targeted protein degradation: expanding the toolbox. *Nat. Rev. Drug Discov.* **18**, 949-963 (2019).
4. Hinterndorfer, M., Spiteri, V. A., Ciulli, A. & Winter, G. E. Targeted protein degradation for cancer therapy. *Nat. Rev. Cancer* **25**, 493-516 (2025).
5. Cyrus, K. *et al.* Impact of linker length on the activity of PROTACs. *Mol. Biosyst.* **7**, 359-364 (2011).
6. Troup, R. I., Fallan, C. & Baud, M. G. Current strategies for the design of PROTAC linkers: a critical review. *ETAT* **1**, 273 (2020).
7. Pike, A. *et al.* Lessons learned in linking PROTACs from discovery to the clinic. *Nat. Rev. Chem.*, 1-16 (2025).
8. Bemis, T. A., La Clair, J. J. & Burkart, M. D. Unraveling the role of linker design in proteolysis targeting chimeras: Miniperspective. *J. Med. Chem.* **64**, 8042-8052 (2021).
9. Steinebach, C. *et al.* Systematic exploration of different E3 ubiquitin ligases: an approach towards potent and selective CDK6 degraders. *Chem. Sci.* **11**, 3474-3486 (2020).
10. Jayarajan, R., Das, J., Bag, S., Chowdhury, R. & Maiti, D. Diverse meta-C− H Functionalization of Arenes across Different Linker Lengths. *Angew. Chem. Int. Ed.* **130**, 7785-7789 (2018).
11. Liu, J. *et al.* Cancer selective target degradation by folate-caged PROTACs. *J. Am. Chem. Soc.* **143**, 7380-7387 (2021).
12. Burslem, G. M., Song, J., Chen, X., Hines, J. & Crews, C. M. Enhancing antiproliferative activity and selectivity of a FLT-3 inhibitor by proteolysis targeting chimera conversion. *J. Am. Chem. Soc.* **140**, 16428-16432 (2018).
13. Imaide, S. *et al.* Trivalent PROTACs enhance protein degradation via combined avidity and cooperativity. *Nat. Chem. Biol.* **17**, 1157-1167 (2021).
14. Cao, Y., Harris, A. L. & Ciulli, A. Branching beyond bifunctional linkers: synthesis of macrocyclic and trivalent PROTACs. *Nat. Protoc.*, 1-36 (2025).
15. Zhou, L. *et al.* DNA framework-engineered chimeras platform enables selectively targeted protein degradation. *Nature commun.* **14**, 4510 (2023).
16. Lebraud, H., Wright, D. J., Johnson, C. N. & Heightman, T. D. Protein degradation by in-cell self-assembly of proteolysis targeting chimeras. *ACS Cent. Sci.* **2**, 927-934 (2016).

17. Santos, T. *et al.* RNA G-quadruplex as supramolecular carrier for cancer-selective delivery. *Eur. J. Pharm. Biopharm.* **142**, 473-479 (2019).
18. Kuzuya, A. *et al.* Allosteric control of nanomechanical DNA origami pinching devices for enhanced target binding. *Chem. Commun.* **53**, 8276-8279 (2017).
19. Kuzuya, A., Sakai, Y., Yamazaki, T., Xu, Y. & Komiyama, M. Nanomechanical DNA origami'single-molecule beacons' directly imaged by atomic force microscopy. *Nature commun.* **2**, 449 (2011).
20. Murat, P., Singh, Y. & Defrancq, E. Methods for investigating G-quadruplex DNA/ligand interactions. *Chem. Soc. Rev.* **40**, 5293-5307 (2011).
21. Ruggiero, E. & Richter, S. N. G-quadruplexes and G-quadruplex ligands: targets and tools in antiviral therapy. *Nucleic Acids Res.* **46**, 3270-3283 (2018).
22. Zhang, S., Wu, Y. & Zhang, W. G-quadruplex structures and their interaction diversity with ligands. *ChemMedChem* **9**, 899-911 (2014).
23. Powell, C. E. *et al.* Chemically induced degradation of anaplastic lymphoma kinase (ALK). *J. Med. Chem.* **61**, 4249-4255 (2018).
24. Zhang, N., Phan, A. T. & Patel, D. J. (3+ 1) Assembly of three human telomeric repeats into an asymmetric dimeric G-quadruplex. *J. Am. Chem. Soc.* **127**, 17277-17285 (2005).
25. Xu, Y., Sato, H., Sannohe, Y., Shinohara, K.-i. & Sugiyama, H. Stable lariat formation based on a G-quadruplex scaffold. *J. Am. Chem. Soc.* **130**, 16470-16471 (2008).
26. Xu, Y., Suzuki, Y., Lönnberg, T. & Komiyama, M. Human telomeric DNA sequence-specific cleaving by G-quadruplex formation. *J. Am. Chem. Soc.* **131**, 2871-2874 (2009).
27. Xu, Y., Ito, K., Suzuki, Y. & Komiyama, M. A 6-mer photocontrolled oligonucleotide as an effective telomerase inhibitor. *J. Am. Chem. Soc.* **132**, 631-637 (2010).
28. Bao, H.-L., Masuzawa, T., Oyoshi, T. & Xu, Y. Oligonucleotides DNA containing 8-trifluoromethyl-2′-deoxyguanosine for observing Z-DNA structure. *Nucleic Acids Res.* **48**, 7041-7051 (2020).
29. Wu, S. *et al.* BRD4 PROTAC degrader ARV-825 inhibits T-cell acute lymphoblastic leukemia by targeting'Undruggable'Myc-pathway genes. *Cancer Cell Int.* **21**, 230 (2021).
30. Winter, G. E. *et al.* Phthalimide conjugation as a strategy for in vivo target protein degradation. *Science* **348**, 1376-1381 (2015).
31. Xu, Y., Ishizuka, T., Kurabayashi, K. & Komiyama, M. Consecutive formation of G-quadruplexes in human telomeric-overhang DNA: a protective capping structure for telomere ends. *Angew. Chem. Int. Ed.* **121**, 7973-7976 (2009).
32. Xu, Y., Kaminaga, K. & Komiyama, M. G-quadruplex formation by human telomeric repeats-containing RNA in Na+ solution. *J. Am. Chem. Soc.* **130**, 11179-11184 (2008).
33. Filippakopoulos, P. *et al.* Selective inhibition of BET bromodomains. *Nature* **468**, 1067-1073 (2010).
34. Fischer, E. S. *et al.* Structure of the DDB1–CRBN E3 ubiquitin ligase in complex with thalidomide. *Nature* **512**, 49-53 (2014).
35. Chen, C. *et al.* Recent advances in pro-PROTAC development to address on-target off-tumor toxicity. *J. Med. Chem.* **66**, 8428-8440 (2023).

36. An, K. *et al.* Stimuli-responsive PROTACs for controlled protein degradation. *Angew. Chem. Int. Ed.* **135**, e202306824 (2023).
37. Yu, D. *et al.* Hydrogen Peroxide-Inducible PROTACs for Targeted Protein Degradation in Cancer Cells. *ChemBioChem* **24**, e202300422 (2023).
38. Liang, C. *et al.* Enzyme-catalyzed activation of pro-PROTAC for cell-selective protein degradation. *Ccs Chemistry* **4**, 3809-3819 (2022).
39. Bi, T. *et al.* Rational design of bioorthogonally activatable PROTAC for tumor-targeted protein degradation. *J. Med. Chem.* **66**, 14843-14852 (2023).
40. Chang, M. *et al.* Bioorthogonal PROTAC prodrugs enabled by on-target activation. *J. Am. Chem. Soc.* **145**, 14155-14163 (2023).
41. Alberti, P. & Mergny, J.-L. DNA duplex–quadruplex exchange as the basis for a nanomolecular machine. *Proc. Natl. Acad. Sci. USA* **100**, 1569-1573 (2003).
42. Yang, F. *et al.* Targeted biomolecule regulation platform: a split-and-mix PROTAC approach. *J. Am. Chem. Soc.* **145**, 7879-7887 (2023).
43. Iida, K., Tera, M., Hirokawa, T., Shin-ya, K. & Nagasawa, K. G-quadruplex recognition by macrocyclic hexaoxazole (6OTD) dimer: greater selectivity than monomer. *Chem. Commun.*, 6481-6483 (2009).
44. Tera, M. *et al.* Macrocyclic hexaoxazoles as sequence-and mode-selective G-quadruplex binders. *Angew. Chem. Int. Ed.* **47**, 5557-5560 (2008).
45. Yasuda, M. *et al.* Target identification of a macrocyclic hexaoxazole G-quadruplex ligand using post-target-binding visualization. *Chem. Commun.* **56**, 12905-12908 (2020).
46. Chung, W. J. *et al.* Solution structure of an intramolecular (3+ 1) human telomeric G-quadruplex bound to a telomestatin derivative. *J. Am. Chem. Soc.* **135**, 13495-13501 (2013).
47. Momotake, A. & Yamamoto, Y. Structural and functional characterization of complexes between heme and dimeric parallel G-quadruplex DNAs. *J. Inorg. Biochem.* **216**, 111336 (2021).
48. Uchiyama, M., Momotake, A., Ikeue, T. & Yamamoto, Y. Stepwise binding of a cationic phthalocyanine derivative to an all parallel-stranded tetrameric G-quadruplex DNA. *J. Inorg. Biochem.* **213**, 111270 (2020).
49. Anantha, N. V., Azam, M. & Sheardy, R. D. Porphyrin binding to quadruplexed T4G4. *Biochemistry* **37**, 2709-2714 (1998).
50. Lu, Q. *et al.* BRD4 degrader ARV-825 produces long-lasting loss of BRD4 protein and exhibits potent efficacy against cholangiocarcinoma cells. *American journal of translational research* **11**, 5728 (2019).
51. Li, Z. *et al.* PROTAC bromodomain inhibitor ARV-825 displays anti-tumor activity in neuroblastoma by repressing expression of MYCN or c-Myc. *Front. Oncol.* **10**, 574525 (2020).
52. Li, Y. *et al.* A G-quadruplex hydrogel via multicomponent self-assembly: formation and zero-order controlled release. *ACS Appl. Mater. Interfaces* **9**, 13056-13067 (2017).
53. Ghosh, T., Biswas, A., Gavel, P. K. & Das, A. K. Engineered dynamic boronate ester-mediated self-healable biocompatible G-quadruplex hydrogels for sustained release of vitamins. *Langmuir* **36**, 1574-1584 (2020).

54. Liu, J. *et al.* Light-induced control of protein destruction by opto-PROTAC. *Sci. Adv.* **6**, eaay5154 (2020).
55. Zheng, M. *et al.* Rational design and synthesis of novel dual PROTACs for simultaneous degradation of EGFR and PARP. *J. Med. Chem.* **64**, 7839-7852 (2021).
56. He, S. *et al.* Aptamer-PROTAC conjugates (APCs) for tumor-specific targeting in breast cancer. *Angew. Chem. Int. Ed.* **133**, 23487-23493 (2021).
57. Patil, K. M. *et al.* G4-PROTAC: targeted degradation of a G-quadruplex binding protein. *Chem. Commun.* **57**, 12816-12819 (2021).
58. Shao, J. *et al.* Destruction of DNA-binding proteins by programmable oligonucleotide PROTAC (O'PROTAC): effective targeting of LEF1 and ERG. *Adv. Sci.* **8**, 2102555 (2021).
59. Ghidini, A., Cléry, A., Halloy, F., Allain, F. H. & Hall, J. RNA-PROTACs: degraders of RNA-binding proteins. *Angew. Chem. Int. Ed.* **133**, 3200-3206 (2021).
60. Nohara, R. *et al.* Degradation of G-Quadruplex-Binding Proteins by G4L-PROTAC via Quaternary Complex Formation. *Angew. Chem. Int. Ed.* **64**, e202515045 (2025).
61. Gao, J. *et al.* A region-confined PROTAC nanoplatform for spatiotemporally tunable protein degradation and enhanced cancer therapy. *Nature commun.* **15**, 6608 (2024).
62. Saraswat, A., Vemana, H. P., Dukhande, V. V. & Patel, K. Galactose-decorated liver tumor-specific nanoliposomes incorporating selective BRD4-targeted PROTAC for hepatocellular carcinoma therapy. *Heliyon* **8** (2022).
63. Xu, Y., Ishizuka, T., Kimura, T. & Komiyama, M. A U-tetrad stabilizes human telomeric RNA G-quadruplex structure. *J. Am. Chem. Soc.* **132**, 7231-7233 (2010).

Acknowledgements
We gratefully acknowledge financial support from the Financial support is from the Japan Society for the Promotion of Science Kakenhi [24K01648],Takeda Science Foundation and JKA SOCIAL ACTION.

Author contributions
Y.X. conceived the project, analyzed data, prepared figures, and wrote the manuscript; S.W. performed experiments, analyzed data and prepared figures; H.S., H.F. and K.N. performed experiments.

Competing interests
The authors declare no competing interests.

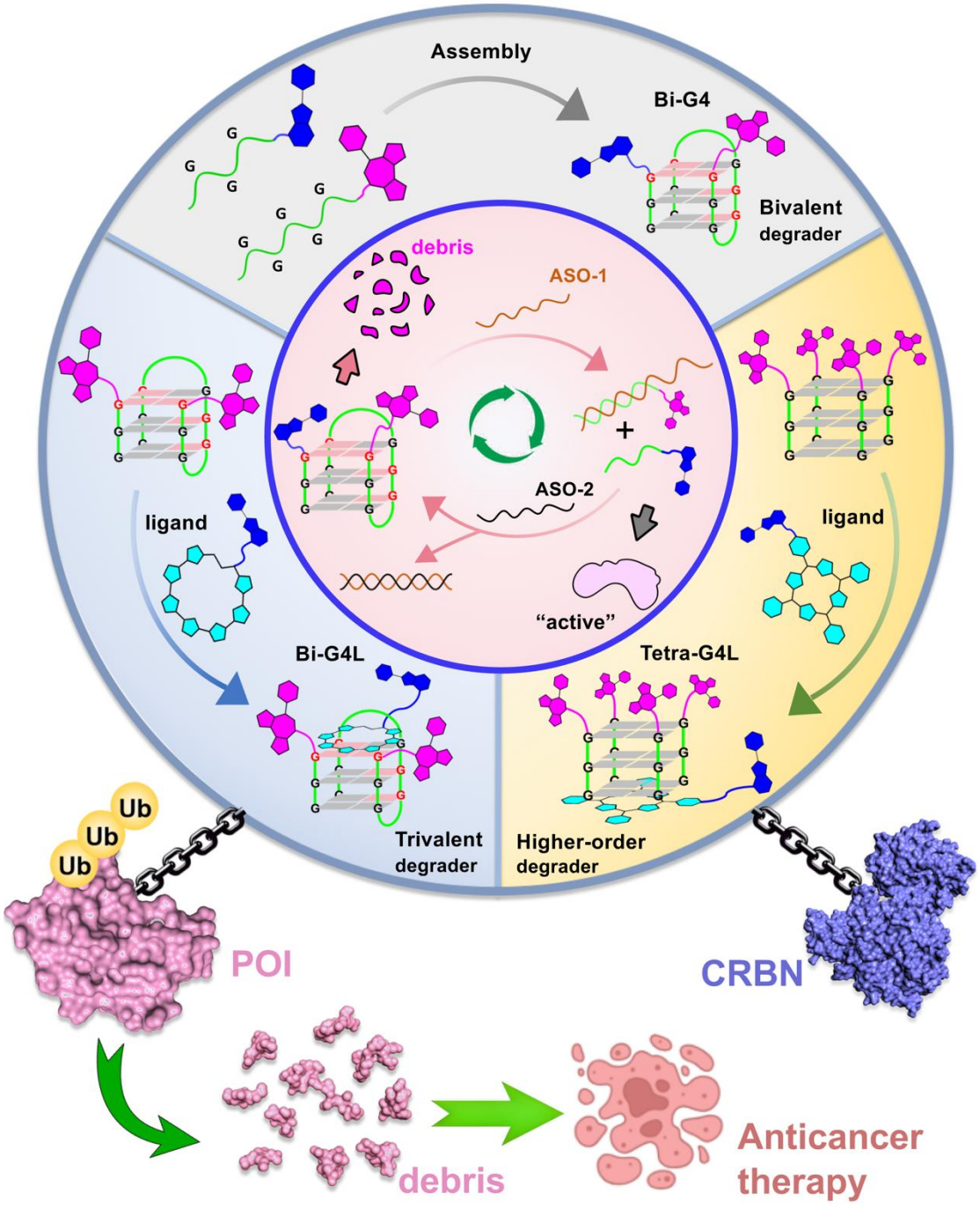
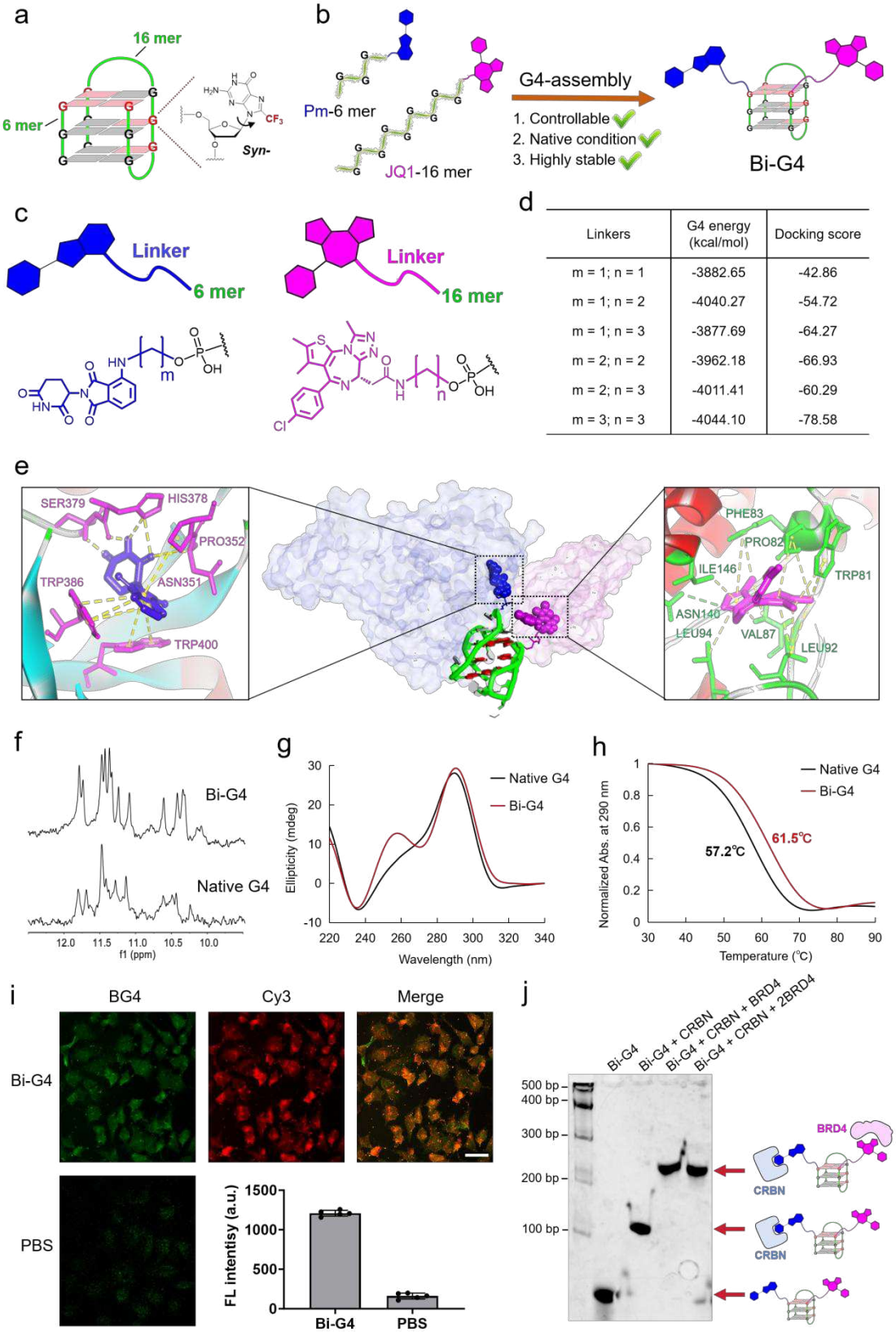


Fig. 1 | Design of the G4TACs platform for selectively targeted protein degradation. The features of the platform is highlighted by the following points: (1) Platform concept of G4 scaffold PROTACs (G4TACs). G-quadruplex (G4) DNA structures serve as modular scaffolds to assemble target-binding ligands and E3 ligase recruiters through a bimolecular G4 framework and G4–ligand interactions, enabling ternary complex formation that triggers ubiquitination and proteasomal degradation of target proteins. (2) Reversible control of protein degradation. Folding and unfolding of the G4 scaffold can be dynamically regulated by antisense oligonucleotides (ASOs), enabling switchable assembly and disassembly of the target protein–G4TAC–E3 ligase ternary complex and thereby providing reversible "on–off" control of protein degradation. (3) Multivalent and programmable platform. The G4 scaffold allows modular and programmable

positioning of multiple ligands, enabling the construction of bivalent, trivalent or higher-order degraders for optimized spatial orientation and enhanced degradation efficiency. (4) *In vivo* therapeutic validation. G4TAC-mediated degradation of oncogenic proteins suppresses tumor growth *in vivo*, demonstrating the potential of this programmable platform for targeted cancer therapy.



Linkers	G4 energy (kcal/mol)	Docking score
m = 1; n = 1	-3882.65	-42.86
m = 1; n = 2	-4040.27	-54.72
m = 1; n = 3	-3877.69	-64.27
m = 2; n = 2	-3962.18	-66.93
m = 2; n = 3	-4011.41	-60.29
m = 3; n = 3	-4044.10	-78.58

Fig. 2 | Synthesis and structural identification of Bi-G4 comprising JQ1 and Pm in G4TACs. **a** A bimolecular G4 structure constructed form a short 6 mer and a longer 16 mer DNA. ^{F}G adopts a *syn* conformation that stabilizes the G4 structure. **b** Pm-6 mer and JQ1-16 mer containing G-rich

sequences spontaneously assemble into a non-covalent G4 structure, forming a functional Bi-G4 degrader for G4TAC applications. **c** JQ1 and Pm were conjugated to the G4-forming oligonucleotides through aliphatic linkers with varying methylene lengths (n). **d** Systematic evaluation of Bi-G4 candidates with different linker lengths, including calculated G4 energies and docking scores for interactions with BRD4 and CRBN. **e** Molecular docking of the Bi-G4–based G4TAC with BRD4 and CRBN. The Pm ligand interacts with ASN351, PRO352, HIS378, SER379, TRP386 and TRP400 of CRBN, whereas JQ1 interacts with TRP81, PRO82, PHE83, VAL87, LEU92, LEU94, ASN140 and ILE146 of BRD4. **f** Imino-proton NMR spectroscopy confirming the formation of Hoogsteen base-paired G-tetrads in Bi-G4 and native G4 (10–12 ppm). **g** CD spectra showing G4 formation of Bi-G4. **h** CD melting analysis showing that Bi-G4 exhibits higher thermal stability (Tm = 61.5 °C) than native G4 (Tm = 57.2 °C). **i** Immunofluorescence imaging of HeLa cells treated with 1 μM Bi-G4 or PBS for 8 h. Bi-G4 was labelled with Cy3 (red), and cellular G4 structures were stained with BG4 antibody (green). Merged images indicate colocalization. Scale bars, 30 μm. Error bars represent mean ± s.d. (n = 5). **j** Native PAGE analysis showing the binding of Bi-G4 to BRD4 and CRBN proteins.

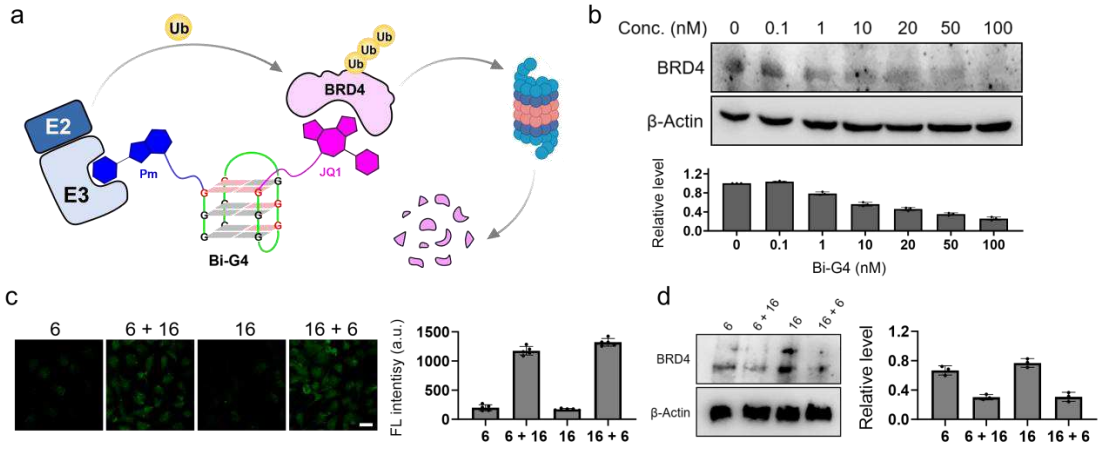


Fig. 3 | Bi-G4 induces BRD4 degradation in HeLa cells. **a** Schematic illustration of Bi-G4–mediated degradation of the protein of interest through ubiquitination and proteasome-dependent degradation. **b** Western blot analysis showing concentration-dependent BRD4 degradation in HeLa cells treated with Bi-G4. **c** BG4 immunofluorescence staining of HeLa cells treated with Pm-6 mer (6), Pm-6 mer + JQ1-16 mer (6 + 16), JQ1-16 mer (16), and JQ1-16 mer + Pm-6 mer (16 + 6). Cellular G4 structures were visualized using BG4 antibody (green; excitation 488 nm, emission 515 nm). Scale bars, 30 μm. **d** Western blot analysis of BRD4 levels in HeLa cells treated with Pm-6 mer (6), Pm-6 mer + JQ1-16 mer (6 + 16), JQ1-16 mer (16), and JQ1-16 mer + Pm-6 mer (16 + 6). Error bars represent mean ± s.d. (n = 3).

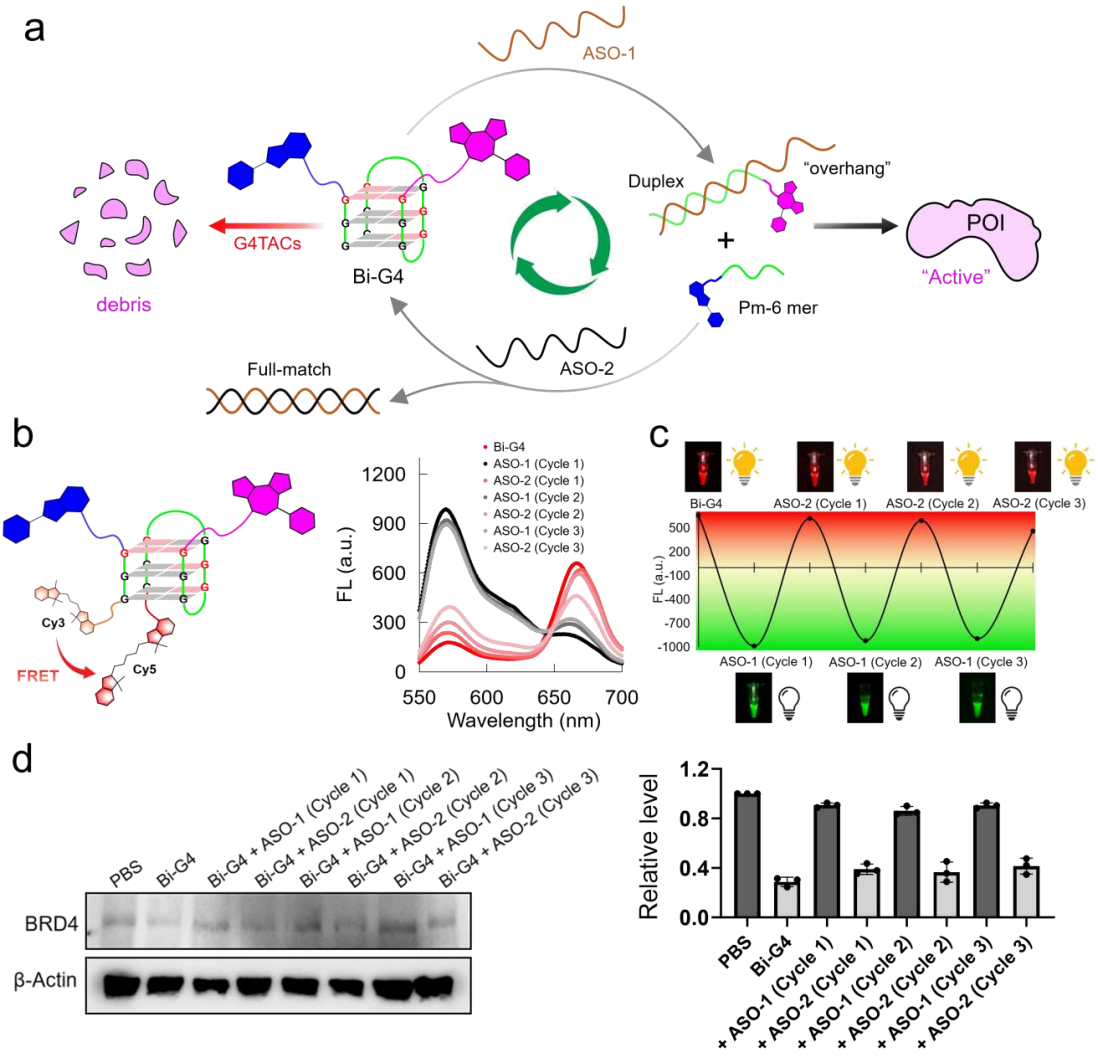


Fig. 4 | Reversible regulation of Bi-G4–induced BRD4 degradation using an ASO strategy. **a** Schematic illustration of reversible switching of protein-of-interest (POI) degradation mediated by Bi-G4 through alternating ASO treatments. ASO-1 disrupts the G4 structure, whereas ASO-2 restores G4 formation, enabling reversible control of Bi-G4 assembly and degradation activity. **b** Left: Cy3 and Cy5 fluorophores were conjugated to the 3′ ends of the 6-mer and 16-mer DNA strands, respectively, to label the G4 structure. Right: Fluorescence spectra showing FRET signals during ASO-mediated switching of Bi-G4 formation (excitation 530 nm). **c** *In vitro* fluorescence imaging showing color changes corresponding to ASO-controlled Bi-G4 structural switching. Green fluorescence arises from the Cy3 channel (excitation 530 nm, emission 570 nm), whereas red fluorescence corresponds to the Cy3–Cy5 FRET channel (excitation 530 nm, emission 670 nm). **d** Western blot analysis showing reversible regulation of BRD4 degradation in HeLa cells upon alternating treatments with ASO-1 and ASO-2 (16 h). Error bars represent mean ± s.d. (n = 3).

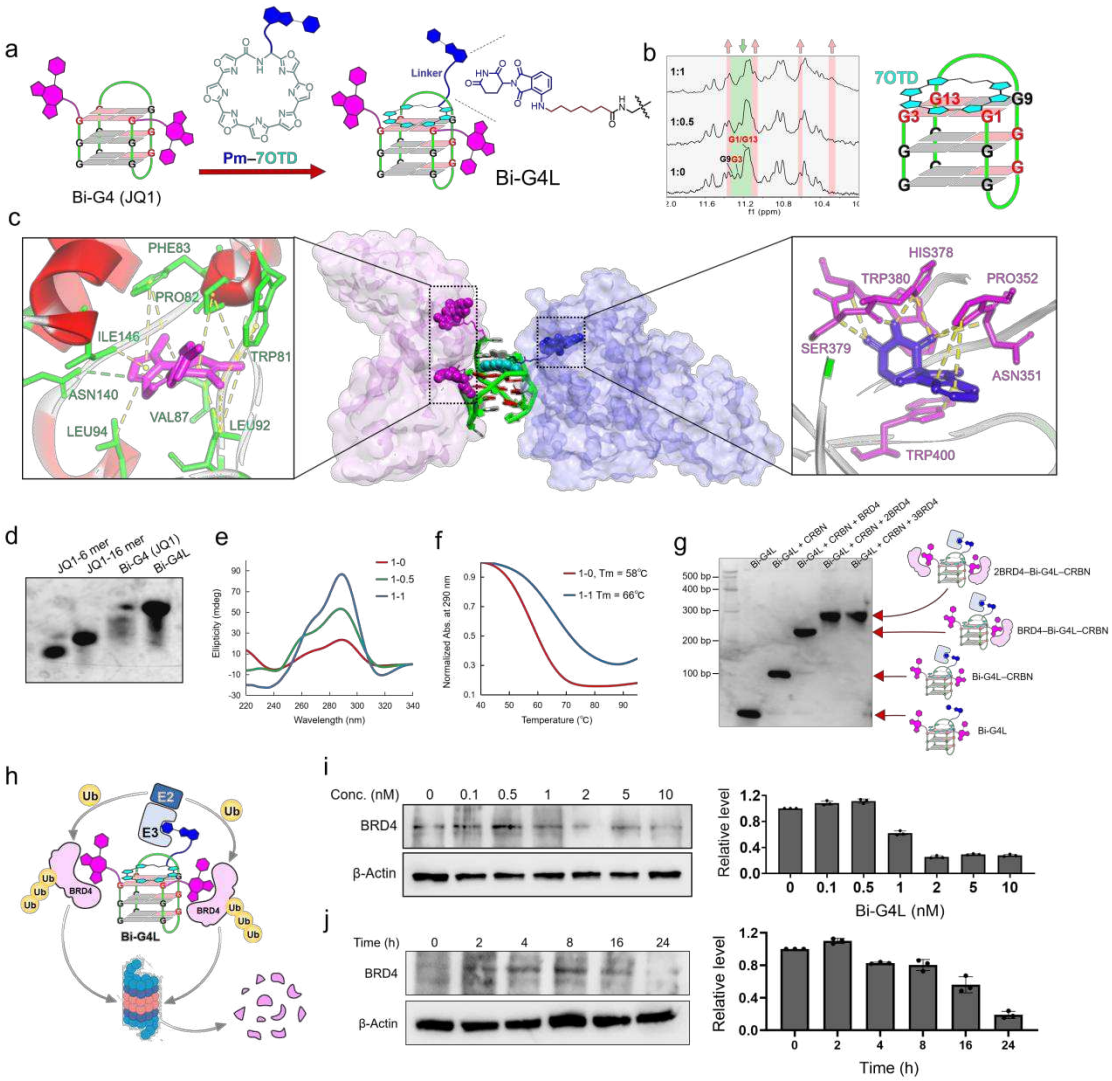


Fig. 5 | Trivalent Bi-G4L enhances BRD4 degradation activity. **a** Schematic illustration of the trivalent Bi-G4L assembly. The G4 ligand Pm-7OTD binds to Bi-G4 (bearing JQ1), forming a trivalent degrader in which Pm and 7OTD are connected by a hexyl linker (n = 3). **b** Imino-proton NMR titration experiments of Bi-G4 with the 7OTD ligand at molar ratios of 1:0, 1:0.5 and 1:1. Signals showing increased or decreased intensities (G1, G3, G9 and G13) are highlighted with red and green backgrounds. Structural model showing 7OTD binding to the G-tetrad formed by G1, G3, G9 and G13 residues based on the NMR results. JQ1 and Pm moieties were omitted to emphasize ligand–G4 interactions. **c** Molecular docking of Bi-G4L with BRD4 and CRBN. The Pm ligand interacts with ASN351, PRO352, HIS378, SER379, TRP380 and TRP400 of CRBN, whereas JQ1 interacts with TRP81, PRO82, PHE83, VAL87, LEU92, LEU94, ASN140 and ILE146 of two BRD4 proteins. **d** Native PAGE analysis confirming formation of the Bi-G4L assembly. **e** CD spectra showing that 7OTD binding to Bi-G4 increases the intensity of the characteristic positive band at 295 nm. **f** CD melting analysis showing that Bi-G4L exhibits higher thermal stability (T_m = 66 °C) than Bi-G4 (T_m = 58 °C; ligand:G4 ratio = 1:1). **g** Native PAGE analysis showing binding of trivalent Bi-G4L to two BRD4 proteins and one CRBN protein. **h** Schematic illustration of Bi-G4L–mediated degradation of the protein of interest through ubiquitination and proteasome-dependent degradation. **i** Western blot analysis showing

concentration-dependent BRD4 degradation in HeLa cells treated with Bi-G4L. **j** Western blot analysis showing time-dependent BRD4 degradation in HeLa cells treated with Bi-G4L. Error bars represent mean ± s.d. (n = 3).

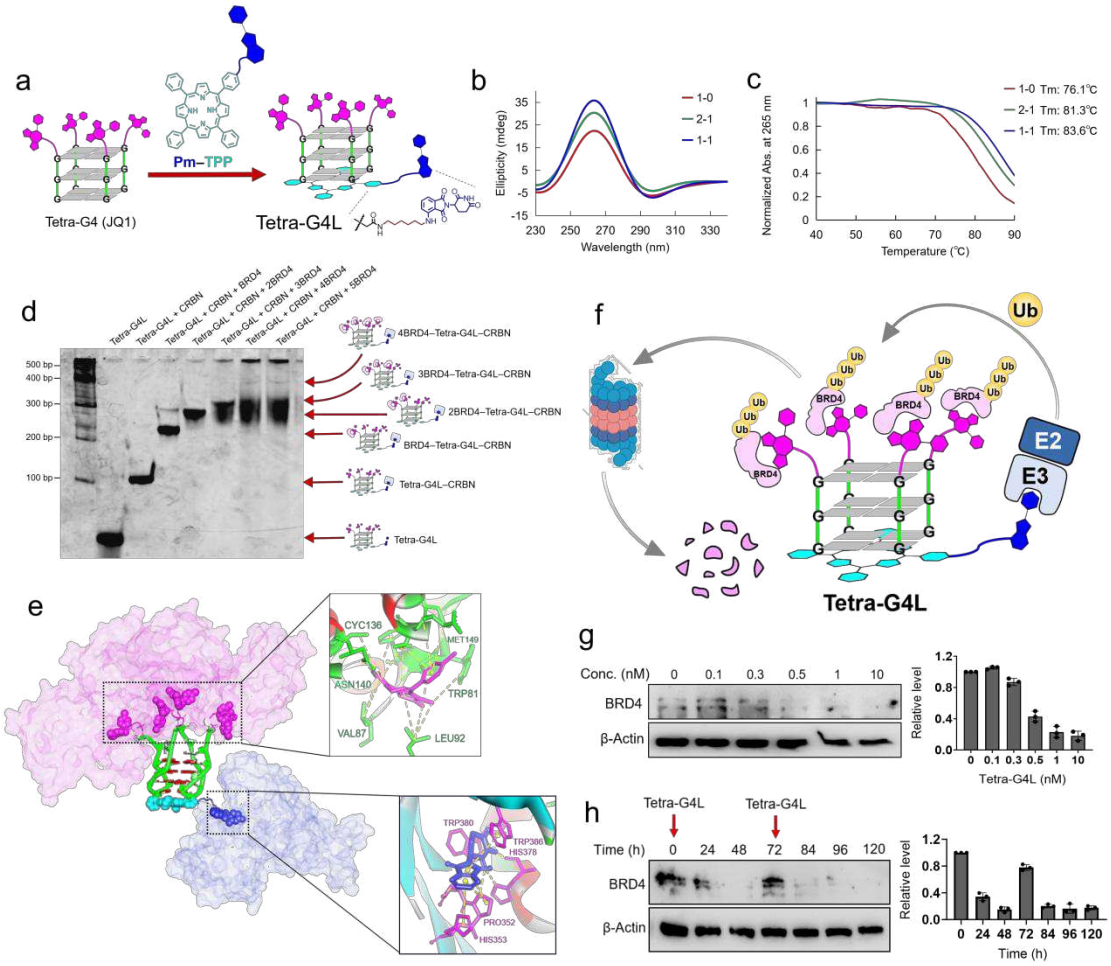


Fig. 6 | Pentavalent Tetra-G4L exhibits enhanced BRD4 degradation activity. **a** Schematic illustration of the pentavalent Tetra-G4L assembly. The G4 ligand Pm–TPP binds to Tetra-G4 (bearing JQ1 ligands) to form a pentavalent degrader, in which Pm and TPP are connected by a hexyl linker (n = 3). **b** CD spectra showing that TPP binding to Tetra-G4 increases the intensity of the characteristic positive band at 265 nm. **c** CD melting analysis showing that Tetra-G4L (ligand:G4 ratio = 1:1) exhibits higher thermal stability (T_m = 83.6 °C) than Bi-G4 (T_m = 76.1 °C). **d** Native PAGE analysis showing binding of pentavalent Tetra-G4L to four BRD4 proteins and one CRBN protein. **e** Molecular docking of Tetra-G4L with BRD4 and CRBN. The Pm ligand interacts with PRO352, HIS353, HIS378, TRP380 and TRP386 of CRBN, whereas JQ1 interacts with TRP81, VAL87, LEU92, CYS136, ASN140 and MET149 of four BRD4 proteins. **f** Schematic illustration of Tetra-G4L–mediated degradation of the protein of interest through ubiquitination and proteasome-dependent degradation. **g** Western blot analysis showing concentration-dependent BRD4 degradation in HeLa cells treated with Tetra-G4L. **h** Time-effectiveness study of Tetra-G4L induced BRD4 degradation in HeLa cells by Western blotting analysis. The error bars indicate the mean ± SD values; n = 3.

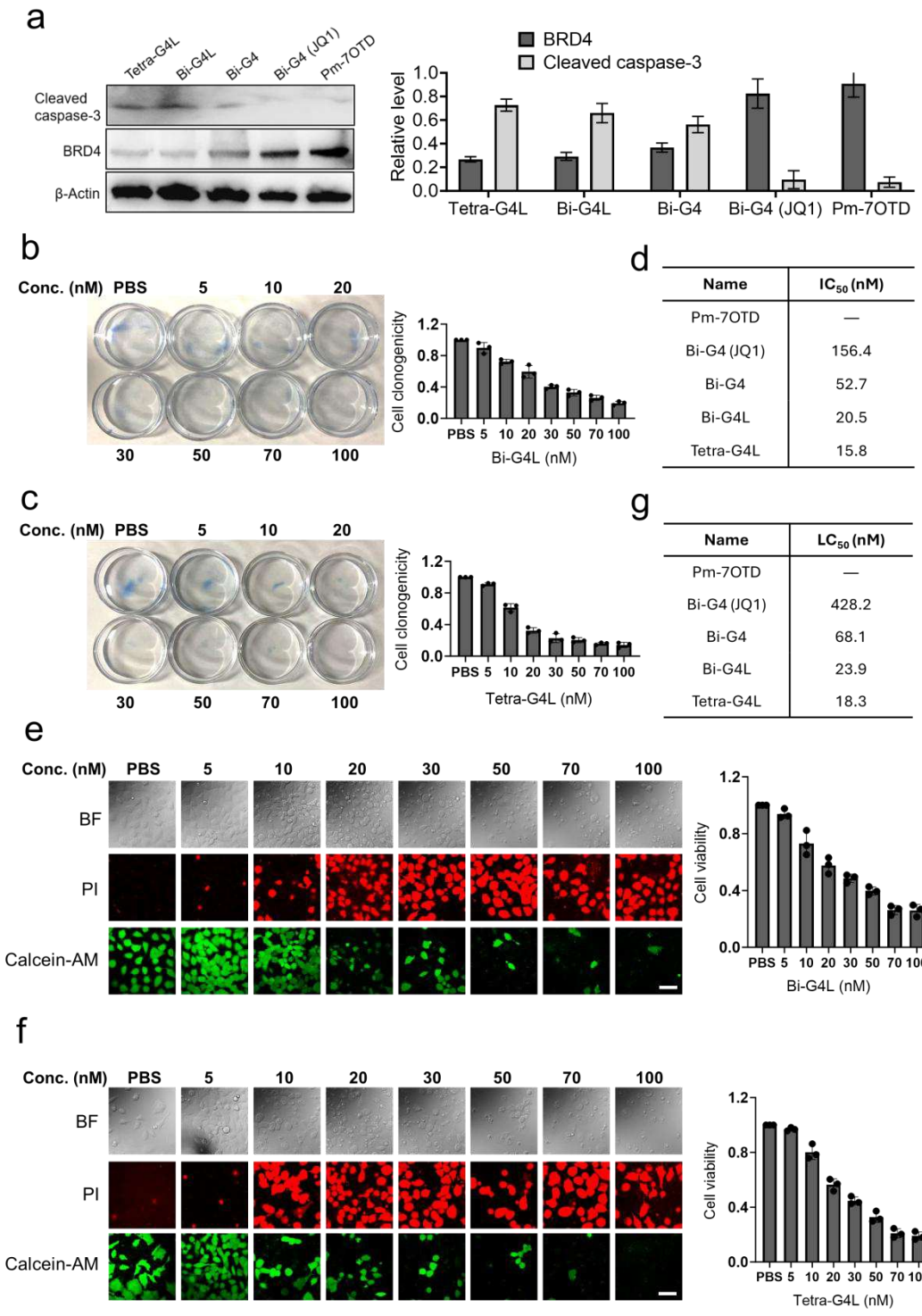


Fig. 7 | G4TACs induce apoptosis and inhibit cancer cell proliferation. **a** Western blot analysis of BRD4 degradation and the apoptosis marker cleaved caspase-3 in HeLa cells treated with Bi-G4, Bi-G4L, Tetra-G4L, Bi-G4 (JQ1) and Pm-7OTD. Error bars represent mean ± s.d. (n = 3). **b** Clonogenic assay of HeLa cells treated with PBS or concentration-dependent Bi-G4L. **c** Clonogenic assay of HeLa cells treated with PBS or concentration-dependent Tetra-G4L. Colonies were stained with methylene blue. **d** Comparison of IC_{50} values of Pm-7OTD, Bi-G4 (JQ1), Bi-G4, Bi-G4L and Tetra-G4L based on cell proliferation inhibition assays. **e** Cell viability assay of HeLa cells treated with PBS or concentration-dependent Bi-G4L. **f** Cell viability assay of HeLa

cells treated with PBS or concentration-dependent Tetra-G4L. Cells were incubated for 72 h before imaging. Live cells were stained with Calcein-AM (green) and dead cells with propidium iodide (PI, red). Scale bars, 60 μm. Error bars represent mean ± s.d. (n = 3). **g** Comparison of LC_{50} values of Pm-7OTD, Bi-G4 (JQ1), Bi-G4, Bi-G4L and Tetra-G4L based on cell viability analysis.

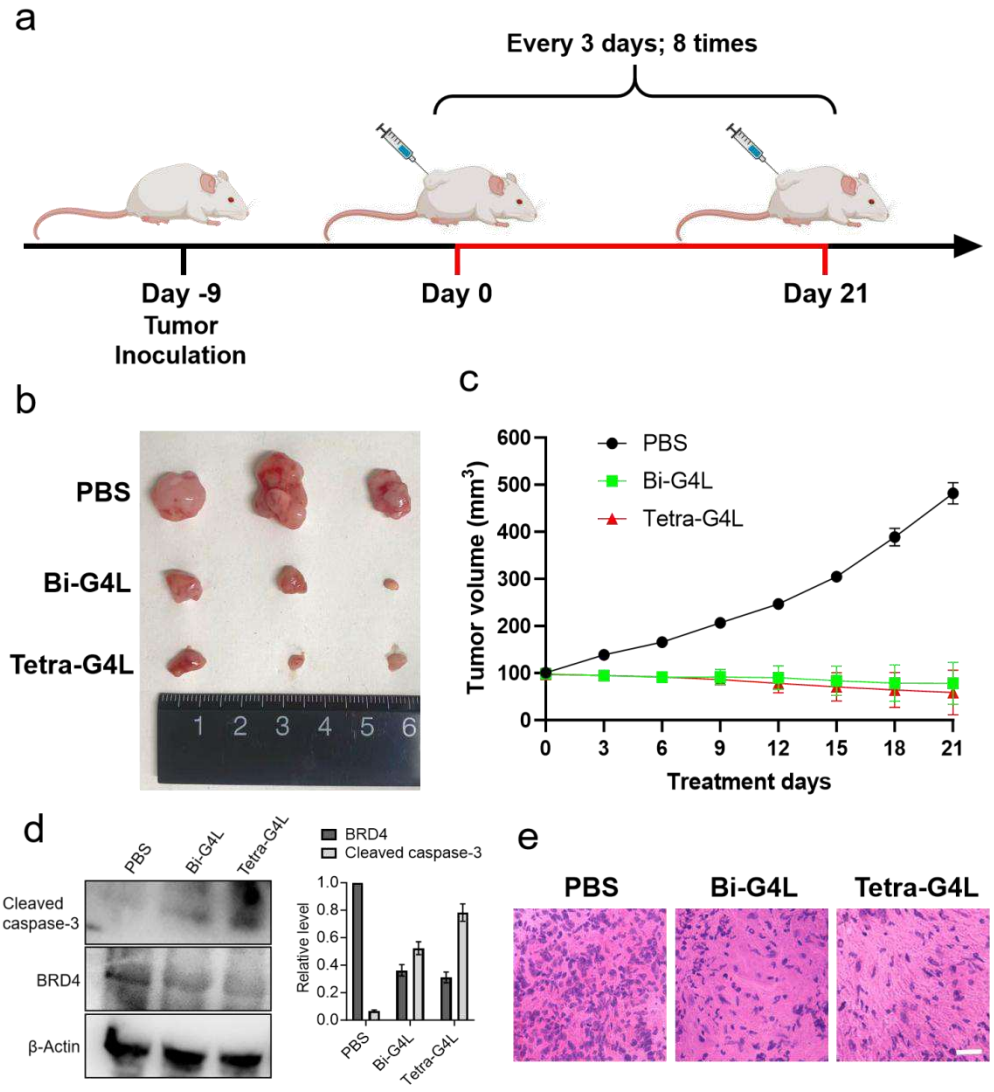


Fig. 8 | G4TACs suppress adrenocortical carcinoma growth *in vivo*.a Schematic illustration of the treatment schedule. Tumour-bearing mice were randomly divided into three groups (n = 3 per group) and treated with PBS, Bi-G4L or Tetra-G4L. **b** Representative images of tumours collected from each group at the experimental endpoint. **c** Tumour growth curves of mice in each group during the 21-day treatment period. Error bars represent mean ± s.d. (n = 3). **d** Western blot analysis of BRD4 and the apoptosis marker cleaved caspase-3 in tumour lysates collected at the endpoint. **e** H&E staining of tumour tissues from each group at the endpoint. Scale bars, 50 μm.

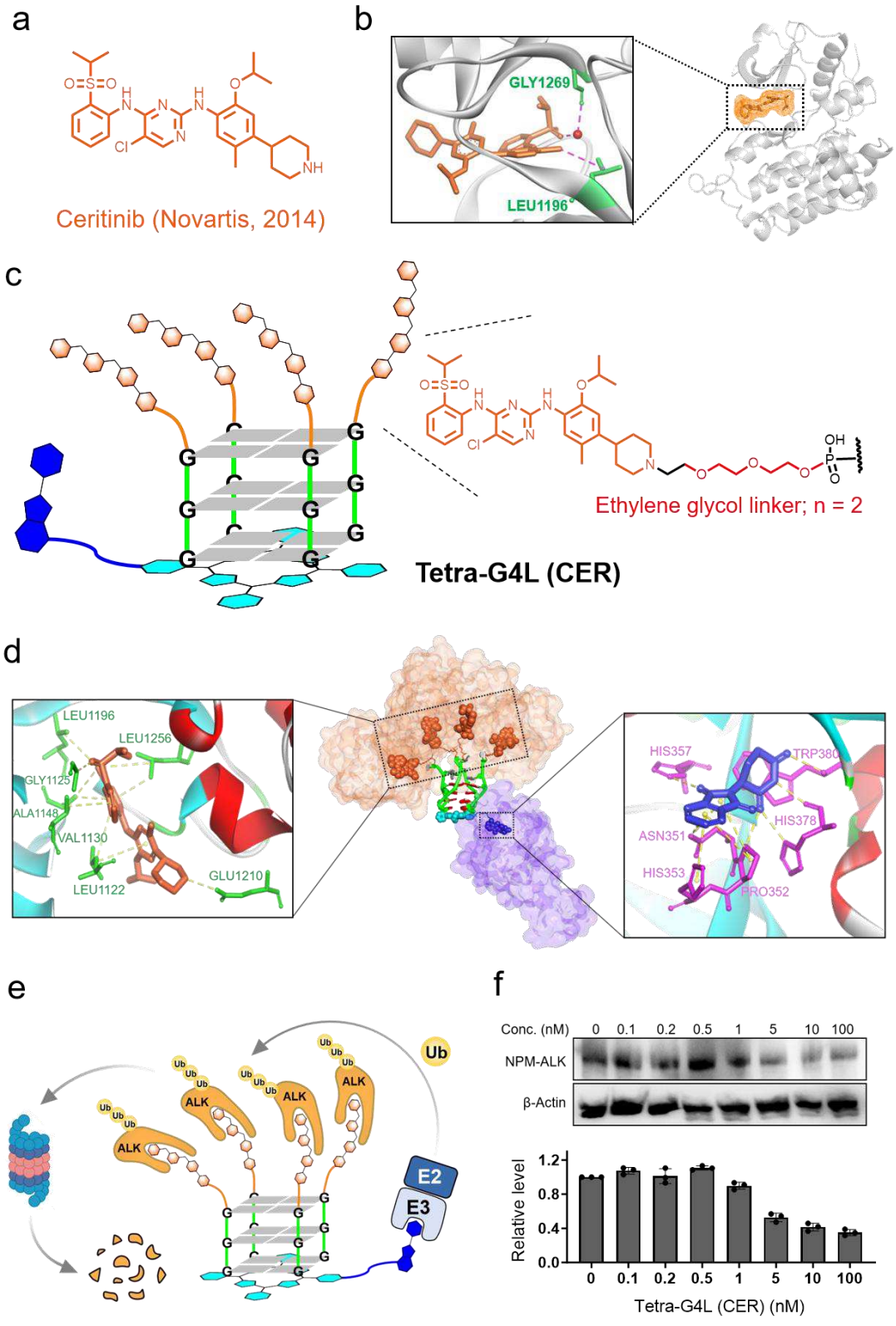


Fig. 9 | G4TACs as a universal platform for degradation of ALK fusion proteins using ceritinib. **a** The ALK inhibitor ceritinib was developed by Novartis and approved by the U.S. Food and Drug Administration in 2014 for the treatment of non-small-cell lung cancer (NSCLC). **b** Reported molecular docking model of ceritinib bound to ALK, showing interactions with

residues G1269 and L1196, which are common mutation sites associated with reduced binding affinity. **c** Construction of Tetra-G4L (CER) using ceritinib linked through a reported ethylene glycol linker (n = 2). **d** Molecular docking of Tetra-G4L (CER) with ALK and CRBN. The Pm ligand interacts withPRO352, HIS353, HIS357, HIS378 and TRP380 of CRBN, whereas ceritinib interacts with LEU1122, GLY1125, VAL1130, ALA1148, LEU1196, GLU1210 and LEU1256 of four ALK proteins. **e** Schematic illustration of Tetra-G4L (CER)–mediated degradation of ALK through ubiquitination and proteasome-dependent degradation. **f** Western blot analysis showing concentration-dependent degradation of NPM-ALK in TK-ALCL1 cells treated with Tetra-G4L (CER). Error bars represent mean ± s.d. (n = 3).

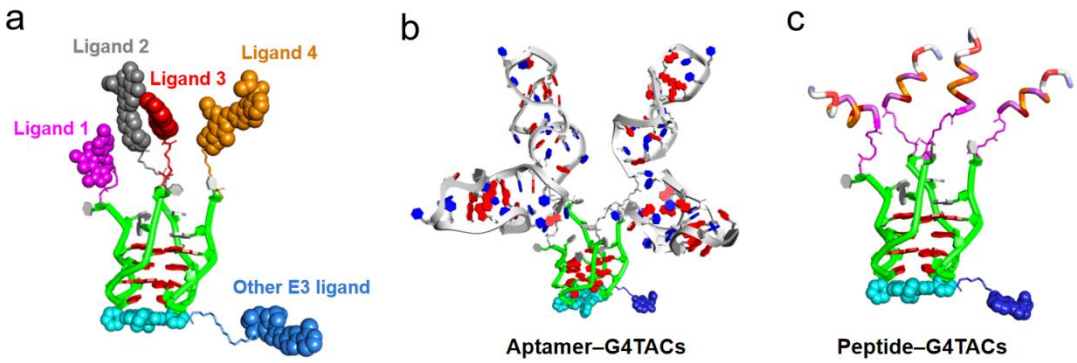


Fig. 10 | Predicted versatility of the G4TAC platform based on computational modelling. **a** All-atom models of G4TAC assemblies constructed using BIOVIA Discovery Studio, illustrating the potential coupling of G4 scaffolds with multiple small-molecule ligands and alternative E3 ligase recruiters (for example VHL). **b** Conceptual design showing that aptamers capable of forming G-quadruplex structures could be used to expand the diversity of G4TAC frameworks. **c** Peptide–G4 conjugates enabling G4TAC-mediated degradation of peptide-binding target proteins.

Supplementary Files

This is a list of supplementary files associated with this preprint. Click to download.

- Supplementaryinformation20260316.docx